14

REAL-TIME TECHNIQUES FOR AERODYNAMIC SIZE MEASUREMENT

PAUL A. BARON

Centers for Disease Control and Prevention,[1] National Institute for Occupational Safety and Health, Cincinnati, Ohio

MALAY K. MAZUMDER

Department of Electrical and Computer Engineering, Boston University, Boston, Massachusetts

YUNG-SUNG CHENG

Lovelace Respiratory Research Institute, Albuquerque, New Mexico

THOMAS M. PETERS

Department of Occupational and Environmental Health, University of Iowa, Iowa City, Iowa

[1]The findings and conclusions in this chapter are those of the authors and do not necessarily represent the views of the Centers for Disease Control and Prevention.

Aerosol Measurement: Principles, Techniques, and Applications, Third Edition. Edited by P. Kulkarni, P. A. Baron, and K. Willeke

14.1 INTRODUCTION

As discussed in the previous chapter, optical particle counting techniques, based on light scattering, have the advantage of rapid, continuous, and nondestructive particle detection. However, the amount of light scattered may not be directly related to a specific property, such as aerodynamic particle size, that one wishes to measure. By combining the advantages of optical detection with the manipulation of particle motion, several instruments have been developed that detect more specific properties, such as aerodynamic size, of aerosol particles. The aerodynamic size of particles is used to describe their behavior in gravitational settling, filtration, respiratory deposition, sampling, and other aerosol systems.

Measurement of aerodynamic size at one time could only be achieved by manually observing settling velocity of individual particles. Subsequently, impactors allowed the measurement of size distributions on a routine basis, although gravimetric and/or chemical analysis still had to be carried out in the laboratory. With the advent of new technology (e.g., lasers and microcomputers), real-time measurements became possible. Several instruments were developed to measure aerodynamic size as rapidly and accurately as possible. These included the Electric-Single Particle Aerodynamic Relaxation Time Analyzer (ESPART; ***HOS***)[2], the Aerodynamic Particle Sizer® (APS; ***TSI***) and the Aerosizer® (***TSI***). While these latter two instruments allow rapid determination of size distributions, they measure particle behavior largely outside the Stokes regime and the recorded size must be corrected to give an accurate aerodynamic size of individual particles.

While the aerodynamic diameter describes the inertial properties, the electrostatic charge influences the electrodynamic behavior of the charged particles in transport processes. Both aerodynamic diameter and electrostatic charge measurements on individual particles are needed in many processes; some examples are electrophotography and laser printing, electrostatic powder coating, electrostatic precipitation, electrostatically enhanced fabric filtration, and electrostatic beneficiation of minerals and coal. The ESPART is capable of measuring particle charge as well as aerodynamic diameter.

These sophisticated instruments provide more specific data about aerosols; however, because of the complexity of their detection and analysis systems, they may also have various limitations and subtle problems associated with the interpretation of the data. The following sections present a discussion of these instruments.

[2]Refer to Appendix I for full manufacturer address indexed to three-letter codes.

14.2 ELECTRIC-SINGLE PARTICLE AERODYNAMIC RELAXATION TIME ANALYZER

14.2.1 Principles of Operation

14.2.1.1 Particle Size and Charge Measurement The ESPART analyzer is based on the motion of particles suspended in a gaseous medium when the particles are subjected to an external oscillatory field. The external field, which can be acoustic, electric, or magnetic, or any combination of these, is applied to oscillate the suspended particles. A Laser Doppler Velocimeter (LDV) is used for measuring the particle motion in the oscillatory excitation field (see Chapter 13). The application of the LDV allows the motion of the particles in response to the applied field(s) to be analyzed in a noncontact manner. The measurements of size and charge of the particles, derived from their relative motion in the gaseous medium, are based on the assumption that the particle motion is within the Stokes's regime, which is valid only when the Reynolds number of the particles' motion is less than 0.1. An oscillating particle suspended in a gaseous medium under the influence of an external acoustic field experiences a drag force which is proportional to the diameter of the particle, given by Stokes' law (Fuchs 1964; Hinds 1999). The drag force, F_D, on a spherical particle,

$$F_D = -3\pi\eta(V_p - U_g)d_p/C_c \qquad \text{(Eq. 14-1)}$$

where η is the coefficient of viscosity of the gaseous medium, V_p is the velocity of the particle relative to the fluid, U_g is the

fluid velocity amplitude, d_p is the diameter of the particle, and C_c is the Cunnigham slip correction factor (see Chapter 2).

Stokes' law assumes that the relative velocity of the gas at the surface of the sphere (boundary layer) is zero, but particles smaller than 1 μm in diameter settle faster than their terminal settling velocity as predicted from Stokes's law. The motion of the fine particles is not continuous under such conditions when molecular slip is a significant factor. A slip correction factor C_c is used to compensate for molecular slips of the small particles. Under the atmospheric condition, $C_c \approx 1.0$ when $d_p \geq 2.0\,\mu m$. The one-dimensional equation of motion of a particle subjected to an external force is given by

$$m_p \frac{dV_p(t)}{dt} + \frac{3\pi\eta d_p}{C_c}(V_p(t) - U_g(t)) = F(t) \qquad \text{(Eq. 14-2)}$$

where, m_p = particle mass, t = time, $F(t)$ is any external force. Rearranging the above equation,

$$\tau_p \frac{dV_p(t)}{dt} + (V_p(t) - U_g(t)) = BF(t) \qquad \text{(Eq. 14-3)}$$

where, $\tau_p = \dfrac{m_p C_c}{3\pi\eta d_p}$, is the relaxation time of the particles, and $B = \dfrac{C_c}{3\pi\eta\, d_p}$ is the mechanical mobility of the particle. When a particle is subjected to a new set of forces, the time required for it to reach 66.7% of its terminal velocity in response to these forces is called the relaxation time. When arbitrary shaped particles are involved, an equivalent aerodynamic diameter (Hinds 1999) is used, the significance of which is discussed later in this chapter. For a spherical particle of density ρ_p the relationship between the geometrical diameter of the particle and its equivalent aerodynamic diameter, d_a, is given as,

$$d_a = d_p(\rho_p/\rho_0)^{1/2} \qquad \text{(Eq. 14-4)}$$

where ρ_p is the density of the particle, and ρ_0 represents unit density, $1\,gm/cm^3$ $[1000\,kg/m^3]$. The relaxation time is related to the aerodynamic diameter and the viscosity of the gaseous medium,

$$\tau_p = \frac{m_p C_c}{3\pi\eta d_p} = \frac{\rho_0 d_a^2 C_c}{18\eta} \qquad \text{(Eq. 14-5)}$$

When a particle is subjected to a sinusoidal acoustic or an electric field, and the external gravitational force $F(t)$ is neglected, the steady state response of the velocity of the particle can be represented as shown in Figure 14-1.

14.2.1.2 Particle Motion in an Acoustic Field Oscillation of a fluid medium induced by a sinusoidal acoustic filed can be represented as

$$U_g(t) = U_g \sin \omega t$$

$F(t) = 0$, then, equation (Eq. 14-3) reduces to

$$\tau_p \frac{dV_{p(a)}}{dt} + V_{p(a)}(t) = U_g \sin \omega t \qquad \text{(Eq. 14-6)}$$

where, $V_{p(a)}$ is the particle velocity amplitude subjected to the acoustic field. Solving the above equation

$$V_{p(a)}(t) = \frac{U_g}{\sqrt{1 + \omega^2 \tau_P^2}} \sin(\omega t - \phi) \qquad \text{(Eq. 14-7)}$$

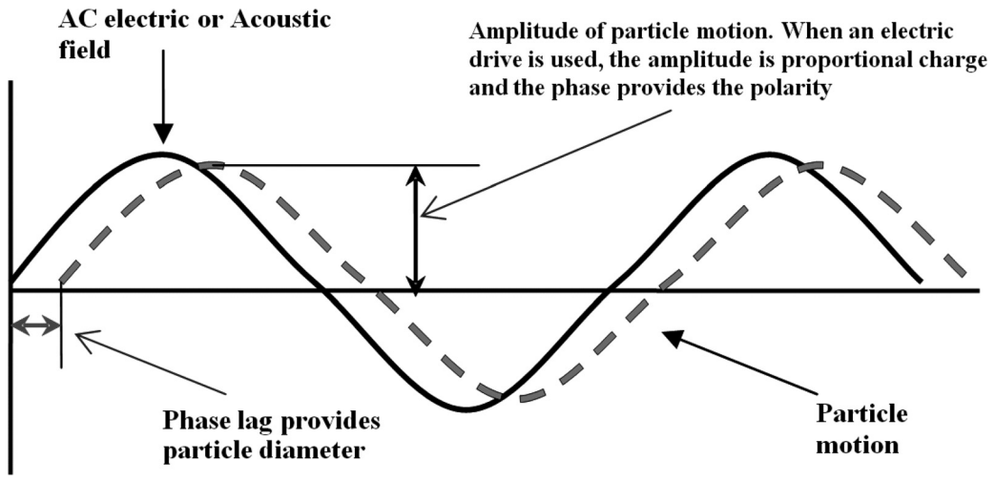

Figure 14-1 Motion of a suspended particle driven by an external sinusoidal electric/acoustic field. In this figure, particle charge is assumed to be negative when an AC electric field used.

where ϕ is the phase lag between the acoustic field of excitation, $U_g \sin \omega t$, at the site of the particle in the sensing volume and the particle velocity $V_{p(a)}(t)$, and is given by

$$\phi = \tan^{-1} \omega\tau_p \qquad \text{(Eq. 14-8)}$$

Figure 14-2 shows the relationship between the phase lag ϕ and the aerodynamic diameter d_a of the particle as a function of the excitation frequency, ω radians/s. In the case of acoustic excitation, there are two major forces acting on the particle beside the gravitational field: (1) the viscous drag force and (2) the force caused by the pressure gradient in the medium at the location of the particle. The first one is caused by the fluid resistance due to the viscosity of the medium and the second is due to the inertial resistance. The effective fluid resistance will depend on the product $\omega\tau_p$. For small values of this product, the fluid resistance is primarily viscous and for large values it is inertial. For sizing aerodynamic diameter, the product $\omega\tau_p$ can vary from 0.01 to 100, depending upon d_a and ω. When $\omega\tau_p$ is in the range 0.01 to 2, the fluid resistance can be approximated by the viscous drag (Eq. 14-1) and when $\omega\tau_p > 2$, both viscous and inertial resistances need to be considered. Equation 14-8 is valid for $\phi \leq 63.5^\circ$ for particle motion when an oscillatory acoustic field is used. For measurements of larger particles, when $\omega\tau_p > 2$, both viscous and inertial resistances may require an appropriate correction term (Fuchs 1964) for Equation 14-1. However, if the excitation frequency is decreased so that the relative phase lag $\phi \leq 63.5^\circ$, the correction term becomes negligible. Alternatively, the ratio of the particle velocity amplitude to the amplitude of the acoustic drive ($V_{p(a)}/U_g$), as shown in Figure 14-3, can be used to determine τ_p or d_a (Kirsch and Mazumder 1975). The correction term can be neglected when the amplitude ratio ($V_{p(a)}/U_g$), as expressed in Equation 14-9, is used for particle sizing.

When an electric field is used for oscillating the particles, Equation 14-8 is valid for the entire range of phase delay. In an acoustic field, particle motion is forced by the pressure gradient of the gas surrounding the particle, whereas in the case of an electric field, the driving electrostatic force is directly applied to the charged particles. In both cases, the particle Reynolds number Re_p is less than 0.1 for $d_a \leq 100$ μm.

The ratio of the particle velocity amplitude to the fluid velocity amplitude (Fig. 14-3) can be expressed from the steady-state solution (for $t \gg \tau_p$) of equation (Eq. 14-6),

$$\frac{V_{p(a)}}{U_g} = \frac{1}{\sqrt{1 + \omega^2 \tau_P^2}} \qquad \text{(Eq. 14-9)}$$

The relaxation time can be determined using either Equation 14-8 or 14-9, as discussed above, from which the particle aerodynamic diameter is calculated. To calculate the ratio ($V_{p(a)}/U_g$), it is necessary to measure both the amplitude of the particle motion and the amplitude of the acoustic field simultaneously unless the value of U_g is constant. A small microphone can be used to measure the acoustic field

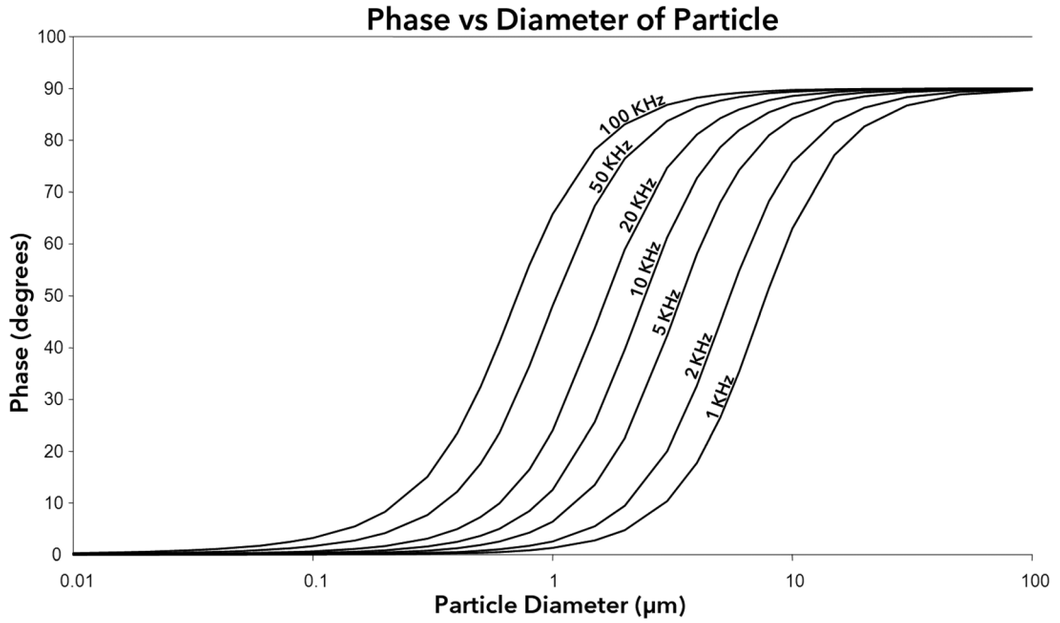

Figure 14-2 Phase lag versus particle aerodynamic diameter with respect to different excitation frequencies driving the particles. The phase plots are valid in the entire range for the electric AC drives at different frequencies as shown. For an acoustic drive, a correction term is needed when $\phi > 63.5^\circ$.

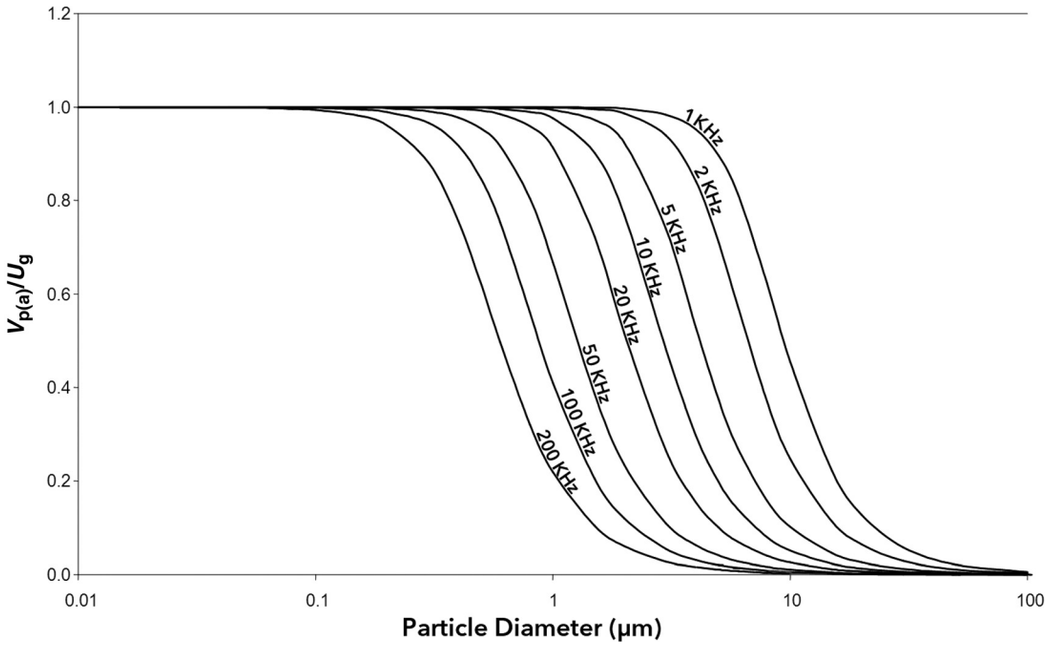

Figure 14-3 Variation in the amplitude ratio of particle velocity to the amplitude of acoustic or electric field of excitation as a function of the aerodynamic diameters of the particles oscillating at different excitation frequencies.

close to the sensing volume. For larger particles, the measurements of the amplitude ratio at a relatively low frequency of acoustic excitation, as shown in Figure 14-3, are advantageous to provide a fairly accurate values of τ_p or $d_{a,}$ since the correction term is negligible for the entire range of the product $\omega\tau_{p.}$

In the ESPART analyzer (Mazumder and Kirsh 1977; Mazumder and Ware 1987; Mazumder et al. 1991; Ali et al. 2008), the relaxation time is generally determined using the phase lag (Eq. 14-8), since it does not require measuring the amplitude of the acoustic field, which may vary as a function of time. The phase lag is independent of the fluctuations of the amplitude of the acoustic field.

The aerodynamic diameter of the particle is given by

$$d_a = \left(\frac{18\eta\tau_P}{\rho_0 C_c}\right)^{1/2} \qquad \text{(Eq. 14-10)}$$

Equation 14-10 shows the relationship between the aerodynamic diameter and the relaxation time. To calculate the aerodynamic diameter from τ_p, it is necessary to know the viscosity of the gaseous medium and the slip correction factor (when $d_a < 2.0\,\mu m$). When the ESPART is used under normal atmospheric condition, the viscosity of air (η) is $1.8134 \times 10^{-5}\,Pa \cdot s$ at a temperature $20\,^{\circ}C$ and this value is taken as a constant unless another ambient condition is used. The slip correction factor C_c, ($C_c \geq 1$), is used when the calculated value of $d_a < 2.0\,\mu m$. When the calculated value of d_a is smaller than $2.0\,\mu m$, and if the specific gravity of the particle, $\rho_p \approx 1$, the slip correction factor (Hinds 1999) can be approximated by

$$C_c = 1 + 2.52\Delta/d_a \qquad \text{(Eq. 14-11)}$$

where Δ is the mean free path of the gas in which the particle is suspended and d_a is the aerodynamic diameter. Under normal atmospheric conditions, the mean free path of air is approximately $0.066\,\mu m$. The ESPART software first calculates d_a assuming $C_c = 1.0$. If the calculated value of $d_a < 2.0\,\mu m$, it recalculates the new value of d_a using Equation 14-11 and the iteration is continued until the calculation converges to a predetermined level of accuracy.

When a different gaseous medium is used and ρ_p is not close to one (since C_c depends upon the geometric diameter), it is necessary to determine the viscosity of the medium, particle density, and the mean free path to calculate the slip correction factor as a function of particle diameter. Since the aerodynamic diameter is measured in the fluid medium in which the particles are suspended, the size distribution measurements are directly related to the gravitational settling velocity and the fluid dynamic properties of the particles in the medium. When an ESPART analyzer was designed for possible use in monitoring atmospheric dust particles on Mars (Srirama et al. 2007; Sharma et al. 2008), it was observed that the changes in atmospheric pressure, temperature, and the composition of the gaseous medium made significant differences in the values of slip correction factor,

relaxation time, Reynolds number, and the resultant phase lag as a function of particle diameter.

14.2.1.3 Particle Motion in an Electric Field When the particles are subjected to a sinusoidal electric field, instead of the acoustic field, the motion of the particles can be analyzed in a similar manner. In this case, $E = E_0 \sin \omega t$, $F(t) = qE$, and $U_g = 0$.

Then, equation (Eq. 14-3) can be rewritten as

$$\tau_p \frac{dV_{p(e)}(t)}{dt} + V_{p(e)}(t) = ZE_0 \sin \omega t \qquad \text{(Eq. 14-12)}$$

where, $Z = qB$, the electric mobility of the particle, q is the charge on the particle, and $V_{p(e)}$ is the particle velocity under the influence of an electric field. Solving Equation 14-12,

$$V_{p(e)}(t) = \frac{ZE_0}{\sqrt{1 + \omega^2 \tau_P^2}} \sin(\omega t - \phi) \qquad \text{(Eq. 14-13)}$$

where

$$\phi = \tan^{-1} \omega \tau_p \qquad \text{(Eq. 14-14)}$$

substituting Z and B in terms of q, and d_a in Equation 14-13, the steady-state solution (for $t \gg \tau_p$) for the amplitude ratio is,

$$\frac{V_{p(e)}}{E_0} = \frac{qC_c}{3\pi\eta d_a \sqrt{1 + \omega^2 \tau_p^2}} \qquad \text{(Eq. 14-15)}$$

From the above Equations 14-14 and 14-15, the aerodynamic diameter, d_a and the electrostatic charge q of the particle are given by (Renninger et al. 1980),

$$d_a = \left(\frac{18\eta\tau_p}{\rho_0 C_c}\right)^{1/2} \qquad \text{(Eq. 14-16)}$$

and

$$q = \frac{V_{p(e)}}{E_0} \frac{3\pi\eta d_a}{C_c} \sqrt{(1 + \omega^2 \tau_p^2)} \qquad \text{(Eq. 14-17)}$$

To determine the charge, q, on a particle, the ratio of the particle velocity amplitude to the amplitude of the electric field is measured. Figure 14-1 shows the motion of a particle due to an AC electric or an acoustic field and the relative phase lag and amplitudes of the particle motion in the oscillatory field of excitation. Figure 14-2 shows the relations between the phase lag and the diameter of the particle for different excitation frequencies. By changing the frequency of the excitation, the range and resolution of size measurement can be varied.

Figure 14-2 is valid for the entire range of phase lag from 0 to 90° when an electric drive is used. Figure 14-3 shows the variations of the amplitude ratio of the particle oscillation ($V_{p(e)}$) to the electric field amplitude (E_0) as a function of particle diameter. The amplitude ratio ($V_{p(e)}/E_0$) measurements provide the magnitude of charge q of the particle once the value of d_a is determined from ϕ. The polarity of the charge q is determined by noting the direction of particle motion relative to the direction of the applied electric field. In an AC field, if the particle is moving toward the positive electrode, the particle has a negative charge ($-q$) and the waveform of particle velocity will be $V_{p(e)} \sin(\omega t - \phi)$ as shown in Figure 14-1. Oscillation of a particle with a positive charge ($+q$) will be 180° out of phase with respect to the electric migration velocity of the negatively charged particle in an AC electric field. The positively charged particles move toward the negative electrode and its motion is represented by $-V_{p(e)} \sin(\omega t - \phi)$.

14.2.1.4 Particle Motion in a DC Electric Field When placed in a DC electric field E_0, the electrostatic force on a charged particle can be expressed as $F_e = qE_0$, where q is the particle charge. A particle of diameter d_a with n elementary charges ($ne = q$), will move with an electrical migration velocity $V_{p(e)}$ given by

$$V_{p(e)} = (qE_0 C_c / 3\pi\eta d_a) \qquad \text{(Eq. 14-18)}$$

In some of the ESPART analyzers, a DC electric field E_0 is applied superimposed to the acoustic field $U_g \sin \omega t$. The particle motion can be represented by $V_{p(a)} \sin(\omega t - \phi) \pm V_{p(e)}$. The sign of $V_{p(e)}$ is considered positive for a negatively charged particle moving to the positive electrode. The DC field E_0 is calculated from the voltage applied across the electrodes divided by the distance between them. In the ESPART analyzer with a DC electric field superimposed on an acoustic excitation, the measurement of $V_{p(e)}$ is used to calculate q, or the number of elementary charges n, once the aerodynamic diameter d_a of the particle has been determined from the phase lag measurement. The software performing the charge measurement reads the voltage (which is adjustable) applied across the electrodes and computes the field E_0 for determining the magnitude of the charge q for each particle. The analyzer also recognizes the direction of particle velocity $V_{p(e)}$ which depends upon the polarity of the charge q of the particle. Thus, from the direction and magnitude of V_e, relative to the applied DC field E_0, the software records both polarity and magnitude of the particle charge q from the equation

$$q = (V_{p(e)} 3\pi\eta d_a)/E_0 C_c \qquad \text{(Eq. 14-19)}$$

The method works well except when the particles are highly charged. The DC field deflects the particles before they reach the LDV sensing volume causing a sampling loss. If the DC electric field intensity is reduced for minimizing the sampling losses, then the resolution of charge measurements is compromised.

It is necessary to reduce sampling losses without sacrificing the resolution while operating the ESPART with DC electric field superimposed on acoustic drive. In order to accomplish this, the ESPART analyzer can be operated in several modes: (1) using an acoustic field for measuring size distributions of charged and uncharged particles; (2) using an AC field for measuring both size and charge distributions for only those particles that are charged; (3) alternating the acoustic and the electric AC fields after a short period (e.g., 5 min) of operation with each drive, to provide the size distributions of both uncharged and charged particles with the acoustic excitation and the size and charge distributions of only charged particles with the AC electric field excitations, respectively; and (4) using both acoustic and AC fields applied synchronously to provide size and charge distributions of the sampled particles in a continuous manner.

14.2.1.5 Real-Time Analysis of Particle Motion Laser Doppler velocimeters (LDV) (Mazumder 1970; Drain 1980; Durst et al. 1981) are used extensively in nonintrusive measurements of fluid flow, turbulence characteristics, and particle dynamics. In the ESPART analyzer, particle motion in an acoustic or in an electric field is analyzed in a noncontact manner using LDV or by image analysis. ESPART analyzers have been built based on both LDV measurements for small particles ($d_a < 50\ \mu m$) and with image analyzers (Mu 1994) for larger particles ($20\ \mu m < d_a < 100\ \mu m$). Most of the instruments now in use are based on the measurement of particle motion with LDV. In the ESPART analyzer, two frequency-biased coherent laser beams are used to measure particle velocity in real time (Mazumder et al. 1979, 1991).

When two coherent laser beams, derived from the same laser, are intersected with each other, an interference fringe pattern is formed, as shown in Figure 14-4. The sensing volume of the ESPART analyzer is formed by this intersection of the two laser beams, which is also the focal volume of the receiving optics of the LDV. When a particle passes through the sensing volume, its scattered light is collected by a photodetector such as a photomultiplier (PMT) or an avalanche photodetector (APD), either in the forward-scattering mode, as shown in Figure 14-4, or in the back-scattering mode. The output of the detector represents Doppler signal bursts generated by each particle passing through the sensing volume. The intensity of the scattered light is not used for size or charge measurements; instead, the ESPART measurements are based on the Doppler shift in the frequency domain, which is used for analyzing particle motion relative to the external drives.

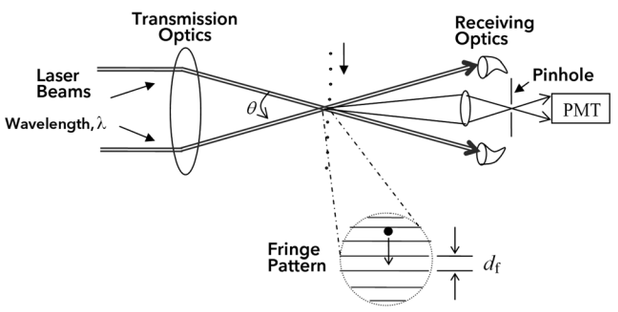

Figure 14-4 Schematic representation of the formation of fringe pattern due to the intersection of laser beams and detection using a photomultiplier tube (PMT).

Figures 14-4 and 14-5 show the optical geometry of the dual-beam frequency-biased LDV used in the ESPART analyzer. The ESPART analyzer, as shown in Figure 14-5, consists of a miniaturized LDV, a particle-sampling chamber, transducers for acoustic and electric drives, an electronic signal and data-processing hardware, and a computer-based digital data acquisition/analysis system (DiVito 1998). The LDV measures the particle velocity as a function of time during the period when the particle is passing through the sensing volume of the LDV. The sensing volume is located within the sampling chamber and between the two pairs of transducers and electrodes, one driven by an acoustic drive and the other by an AC electric field. The particles are subjected to an acoustic or/and an electric excitation field as they transit through the sensing volume.

Commercially available ESPART analyzers (**HOS**) use a DC electric field (E_0) superimposed on an acoustic field $U_g \sin \omega t$ with an excitation frequency of 2.0 kHz. The excitation field at a given frequency causes the particles to undergo sinusoidal oscillations. When a DC electric field is superimposed on an acoustic field, the velocity of a charged particle will have an oscillatory component superimposed on its electrical migration velocity $V_{p(e)}$ (Eq. 14-18), which can be expressed as,

$$V_{pm} = V_{p(a)} \sin(\omega t - \phi) + V_{p(e)} \qquad \text{(Eq. 14-20)}$$

for a DC field E_0, and, when both acoustic and AC electric fields are applied synchronously,

$$V_{pm} = V_{p(a)} \sin(\omega t - \phi) \pm V_{p(e)} \sin(\omega t - \phi) \qquad \text{(Eq. 14-21)}$$

The positive sign is used when q is negative (negatively charged particles move towards the positive electrode) and the sign is negative when q is positive.

As a particle passes through the sensing volume in the direction normal to the plane containing the two converging laser beams, the particle experiences an acoustic and/or an electric field. The LDV detects only the horizontal velocity component of the particle. It does not detect the vertically downward sampling velocity. However, the duration of the LDV signal burst depends upon the residence time of the particle within the sensing volume and it is inversely proportional to the sampling velocity. The residence time must be long enough to measure ϕ for computing the particle aerodynamic diameter d_a and the amplitude ratio $(V_{p(e)}/E_0)$ for

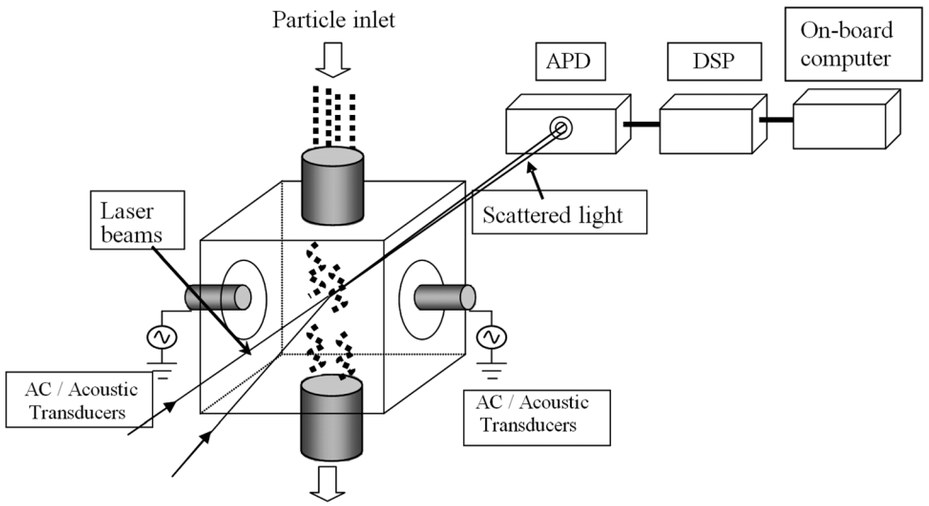

Figure 14-5 A three-dimensional view of the ESPART Analyzer showing noncontact particle size and charge measurements using a laser Doppler velocimeter, a particle sampling chamber, and an electronic signal processor for computing particle size and charge from the scattered Doppler signals from individual particles.

computing the magnitude of the particle charge q. (Kirsch and Mazumder 1975; Mazumder et al. 1991). The polarity of the charge q is determined by detecting if the electrical migration velocity of the particle is positive (q is negative) or negative (q is positive). In this manner, both particle size and electrostatic charge (magnitude and polarity) are determined on a single particle basis and the distribution is stored in the computer. The commercially available instrument is used primarily for analyzing the electrophotographic properties of toner used in laser printers and copiers.

14.2.1.6 Acoustic versus Electric Excitation Field When subjected to an acoustic drive, both the phase lag and the amplitude ratio of particle motion provide the same size information. The acoustic drive mode of operation provides the size distribution of particles regardless of whether the particle is charged or uncharged. The AC drive mode works only when the particles are charged and provides both size and charge information of the charged particles. Each ESPART instrument can be operated either using the acoustic or electric drive. As discussed before, operating the ESPART analyzer by alternating the acoustic and AC drives after short time intervals (e.g., 5 min), it is possible to measure both size and charge distributions and the fraction of the particles in the sample that are charged. This sequential operation can be used for characterizing an aerosol if the particle size and charge distributions are stable during the time period of measurements. The ESPART analyzer can also be operated with both acoustic and AC drives applied synchronously (Eq. 14-21). The experimental arrangement used for the ESPART Analyzer with acoustic, AC, or the synchronous AC and acoustic drives for measuring both size and charge distributions is shown in Figure 14-6.

14.2.2 Electric-Single Particle Aerodynamic Relaxation Time Analyzer Operation with Synchronous Acoustic and Electric Drives

Under this condition, the particle velocity component due to the acoustic drive, $V_{p(a)} \sin(\omega t - \phi)$, is superimposed, in phase, on its electrical migration velocity $V_{p(e)} \sin(\omega t - \phi)$ for a negatively charged particle (Eq. 14-21, Fig. 14-7). For a positively charged particle, there is a 180° phase lag between the two components, and the electrical migration velocity can be expressed as $-V_{p(e)} \sin(\omega t - \phi)$. The amplitude of electrical migration velocity, $V_{p(e)}$ is given by the equation (Eq. 14-18).

In the previous sections, we have shown that for sinusoidal external forces the phase lag between the oscillation of the particle and that of the excitation force is related to the relaxation time τ_p and the frequency of oscillation. The phase lag (ϕ) is related to τ_p by $\phi = \tan^{-1} \omega\tau_p$.

The relaxation time τ_p can also be determined by measuring the amplitude ratio of the particle velocity and the amplitude of the acoustic excitation,

$$\frac{V_{p(a)}}{U_g} = \frac{1}{\sqrt{1 + \omega^2 \tau_p^2}}$$

The aerodynamic diameter (d_a) can be determined from the relaxation time using the equation

$$d_a = \left(\frac{18\eta\tau_p}{\rho_0 C_c}\right)^{1/2}$$

If the particle has an electrostatic charge (q), the amplitude ratio of the particle velocity to the AC electric field is given by

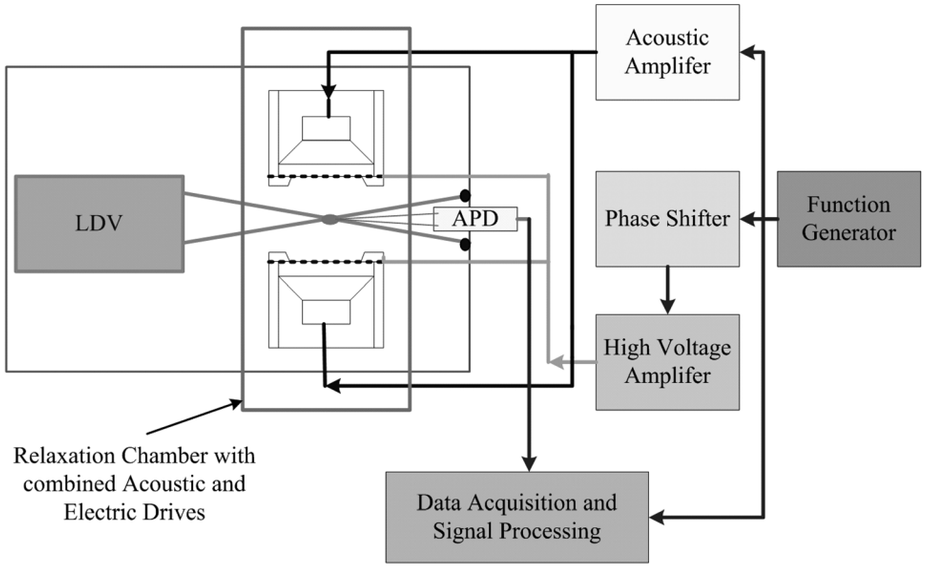

Figure 14-6 Experimental setup of the ESPART analyzer for operating with acoustic, electric, or synchronous operation of acoustic and electric drives for measuring particle size and electrostatic charge distributions.

$$\frac{V_{p(e)}}{E_0} = \frac{qC_c}{3\pi\eta d_a\sqrt{1+\omega^2\tau_p^2}}$$

When both the acoustic and electric fields are superimposed, the particle motion $V_{p(m)}$, will be the vector sum of the two velocity components. When the fields are synchronous, the two velocity component waveforms will be superimposed on each other as shown in Figure 14-7. The measured particle velocity amplitude $V_{p(m)}$, is the sum of the two superimposed particle velocity amplitudes ($V_{p(a)} + V_{p(e)}$). If $V_{p(a)}$ is known, it is possible to determine $V_{p(e)}$ to compute the particle charge q

$$q = \frac{V_{p(e)}3\pi\eta d_a\sqrt{1+\omega^2\tau_p^2}}{E_0 C_c} \qquad \text{(Eq. 14-22)}$$

Since,

$$V_{p(e)} = V_{p(m)} - V_{p(a)} \qquad \text{(Eq. 14-23)}$$

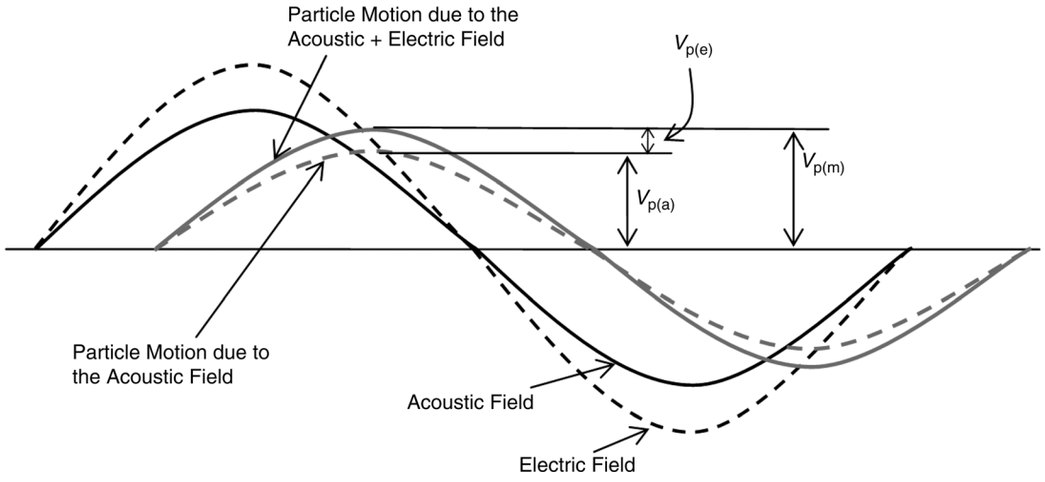

Figure 14-7 Particle motion in synchronous acoustic and electric fields; the phase lag of the particle with respect to the two superimposed fields is the same while the amplitude of the particle velocity is the sum of the two amplitudes. The polarity of the particle charge is negative since $V_{p(e)}$ is positive.

and the particle velocity amplitude $V_{p(a)}$ can be derived from the phase lag (ϕ), using the relationship

$$V_{p(a)} = \frac{U_g}{\sqrt{1 + \omega^2 \tau_p^2}} = \frac{U_g}{\sqrt{1 + (\tan \phi)^2}} \qquad \text{(Eq. 14-24)}$$

and

$$\phi = \tan^{-1} \omega \tau_p \qquad \text{(Eq. 14-25)}$$

where η is the coefficient of viscosity of the medium, C_c is the Cunningham slip correction factor, ω is the frequency of excitation in radians per second, and U_g is the amplitude of the applied acoustic field. Figure 14-7 shows that the acoustic field (shown in solid line) and the electric field (shown in broken line) are applied simultaneously in a synchronous manner forcing the particle, placed in the sensing volume of the instrument (Fig. 14-6), to oscillate. The resultant particle motion due to the two applied fields of excitation is shown in solid line. This oscillatory motion of the particle will be measured by the detector as the particle velocity as a function of time. Since, for a given frequency, the phase lag ϕ of the particle motion is same for both acoustic and electric drives, and since the amplitude of the particle velocity depends upon acoustic velocity amplitude U_g, it is possible to determine the particle velocity response due only to the acoustic drive. The broken line of the particle response curve in Figure 14-7 shows the calculated particle velocity profile for the acoustic drive. Since the measured velocity amplitude is higher than the calculated velocity amplitude $V_{p(a)}$, the polarity of the particle charge is negative (Eq. 14-20). In Figure 14-8, the excitation fields are same as shown in Figure 14-7, but in this case the measured particle velocity amplitude (shown as solid line) is lower than the calculated velocity amplitude when only the acoustic field of excitation is present. Therefore, the polarity of the particle charge is positive (Eq. 14-21).

If the amplitude of the acoustic drive, U_g, is constant or is measured by using a microphone, it is possible to determine $V_{p(a)}$ from τ_p using the equation (Eq. 14-24). The ESPART software first computes τ_p from the measured value ϕ and the aerodynamic diameter is determined. It then computes the value of $V_{p(a).}$ Using the equation (Eq. 14-23) the value of $V_{p(e)}$ is derived and the charge q is then determined from the equation (Eq. 14-22).

Determination of U_g with an acoustic microphone requires that the microphone be placed very close to the position of the sensing volume. The placement of the microphone close to the sensing volume can interfere with the electric and acoustic fields. It is also possible to measure U_g in a nonintrusive manner by using the ESPART LDV to measure the velocity amplitude $V_{p(a)}$ of a particle of known size driven at a known frequency. For example, using only the acoustic drive at a frequency of 1.0 kHz, with fairly monodispersed particles with d_a between 1 to 2 μm in diameter, the measured $V_{p(m)}$ will be within 99.98–99.66% of U_g from theoretical calculation (Eq. 14-9) as shown in Figure 14-3. If a microphone is placed at a convenient location close to the sensing volume, its output can be calibrated from the LDV measurements of U_g as long as the frequency of the acoustic drive is not changed. If the microphone output remains constant when the ESPART is operated at the same frequency, the value of U_g can be assumed constant. The calibration procedure needs to be repeated if the frequency of operation is changed.

The steps for measurement of charged and uncharged particles with simultaneous application of acoustic and electric field can be summarized as follows:

1. Measurement of U_g: Using monodisperse aerosol particles in the size range 1- to 2-μm diameter of

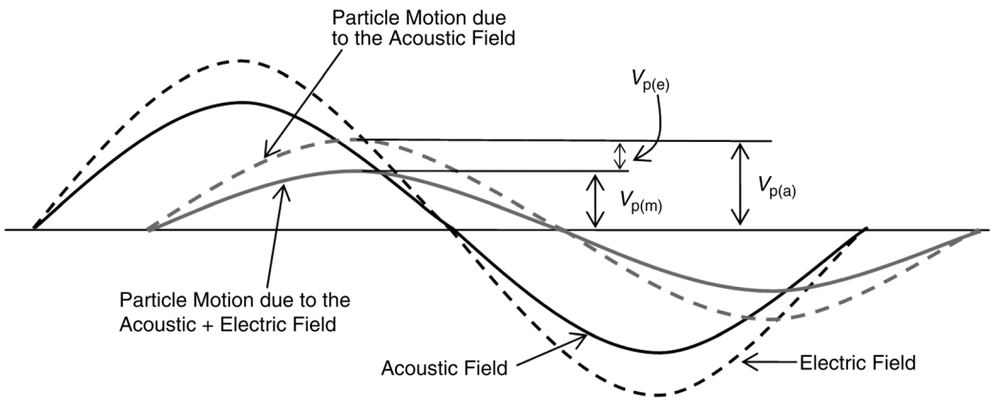

Figure 14-8 Particle motion in synchronous acoustic and electric fields; the phase lag of the particle with respect to the two superimposed fields is same while the amplitude of the particle velocity is the sum of the two amplitudes. The polarity of the particle charge is positive since $V_{p(e)}$ is negative.

polystyrene latex spheres (PLS) and applying only the acoustic drive, the measured value $V_{p(a)}$ is used to determine the acoustic drive amplitude, U_g, at the desired frequency of the acoustic drive. A small microphone is placed close to the LDV sensing volume (without interfering with the acoustic and electric fields), and the microphone output is calibrated for different frequencies (>1.0 kHz) of operation.

2. Measurements of $V_{p(m)}$, ϕ, d_a, and $V_{p(a)}$: Under the synchronous application of the acoustic and electric fields, as shown in Figure 14-7, the phase lag ϕ is determined for each particle as it passes through the sensing volume. The aerodynamic diameter d_a is then calculated from ϕ. The microphone output is read and, if there is no change, the acoustic velocity amplitude U_g is assumed constant and the particle velocity amplitude $V_{p(a)}$ is calculated. The value of $V_{p(a)}$ is then compared to the measured value of particle amplitude $V_{p(m)}$ for determining the particle charge q.
3. Measurement of particle charge q: When the measured value of the velocity amplitude $V_{p(m)}$ ($V_{p(a)} \pm V_{p(e)}$) is larger than the calculated particle velocity amplitude due to the acoustic drive $V_{p(a)}$, the value of $V_{p(e)}$ (due to the electric field) is positive. The polarity of the charge q is negative and its magnitude is calculated by first subtracting $V_{p(a)}$ from $V_{p(m)}$ and the value of q is calculated by using Equation 14-22. In this case, the polarity of the particle charge is negative, as shown in Figure 14-7.

   When the particle charge is positive, the measured value of the amplitude $V_{p(m)}$ will be smaller than the calculated value of $V_{p(a)}$. Under this case,

$$V_{p(m)} = V_{p(a)} - V_{p(e)} \qquad \text{(Eq. 14-26)}$$

   the value of $V_{p(e)}$ is determined by subtracting $V_{p(a)}$ from $V_{p(m)}$; it will be negative as shown in Equation 14-23, indicating the particle charge is positive.

   When the calculated $V_{p(a)}$ is equal to the measured $V_{p(m)}$, this condition indicates that the particle is neutral or the electrostatic charge q is very close to zero, since the electric field did not have any measurable effect.

$$V_{p(m)} = V_{p(a)}, \quad V_{p(e)} = 0, \quad \text{and} \quad q = 0 \qquad \text{(Eq. 14-27)}$$

The synchronous mode of measurements of d_a and q for each particle assumes that the two drives are adjusted to have $V_{p(a)} \gg V_{p(e)}$. It is desired that the two drives do not oppose each other (when q is positive) to the extent resulting $V_{p(m)} = 0$. The Equation 14-22 shows that if $V_{p(a)} = V_{p(e)}$, $V_{p(m)}(t) = 0$ and there will be no oscillatory motion of the particle. When particle velocity amplitude $V_{p(m)}$ approaches zero, the phase lag measurements will be increasingly difficult, as $V_{p(m)} \to 0$, making the instrument inoperative for size and charge measurements. A relatively large value of particle velocity amplitude $V_{p(m)}$ is desired for accurate measurements of size and charge. This is realized by applying the acoustic drive strong enough to have $V_{p(a)} \gg V_{p(e)}$ without sacrificing the range and resolution of particle charge measurements.

14.2.3 Electric-Single Particle Aerodynamic Relaxation Time Analyzer: Current Performance

14.2.3.1 Measurement Aerodynamic Size Distributions of Liquid Droplets and Solid Particles The ESPART analyzer measures the aerodynamic size distribution of solid particles and liquid droplets. The aerodynamic diameter d_a, by definition, is the equivalent diameter of a unit-density solid particle (or liquid droplet) that has the same settling velocity as the particle in question. Aerodynamic diameter is the most commonly used equivalent diameter of particles when fluid dynamics or electrodynamics of the particles are investigated. Examples of such investigations are: settling velocity of atmospheric particles under gravity, lung deposition of inhaled aerosol particles, movement of toner particles in copying machines, electrostatic powder coating, and mixing and dispersion of fine pharmaceutical powders. Aerodynamic diameter takes into account geometrical size and shape and particle density and surface characteristics; it is independent of non-size-related properties such as optical scattering and absorption properties and chemical composition. The ESPART analyzer can be used for both solid particles and liquid droplets (Mazumder et al. 1983, 1999; Ali et al. 2008) and the measurements can be made *in situ*.

14.2.3.2 Electric-Single Particle Aerodynamic Relaxation Time Analyzer versus Optical Particle Counters: Calibration and Coincidence Another equivalent diameter of particles commonly used is the optical diameter, based on the light-scattering properties of the particles being measured. Optical diameters are relevant when optical scattering properties, such as visibility and light absorption measurements are needed. Optical particle counters (OPC) are extensively used for rapid and remote size distribution measurements of particles. However, since the scattering properties of the particles are dependent on the physical size, chemical composition, color, and surface features of the particles, extensive calibration is needed for each application. It is difficult to get accurate size distribution information when particles of different optical properties are involved in the same application. The OPC also suffers from coincidence errors in that the particle size is inferred from the intensity of the scattered light received from the particle(s) present in the sensing volume. When more than one particle is present in the sensing volume, the OPC recognizes it as a large particle, giving a wrong size information.

Like the OPC, ESPART analyzers are also single particle, noncontact-size measuring instruments. In the ESPART analyzer, the Doppler shift in frequency is measured as long as the intensity of the scattered light is sufficiently high to provide a good signal-to-noise ratio. The actual intensity of the light is not measured. When more than one particle is present in the sensing volume, the signal-to-noise ratio of the Doppler signal becomes very poor because of the interference between the signals arising from different particles and the signal is rejected. Thus the size information is lost but wrong information is not given. To minimize the coincidence loss in the particle concentration measurements, the sensing volume of the ESPART analyzer is made very small, on the order of 10^{-12} m^3. For most applications, the coincidence error is minimal. As discussed before, the ESPART measurement is based on the principle that the aerodynamic diameter of individual particles is measured regardless of chemical composition, particle density, color, and surface feature. If all the instrumental parameters and the environmental conditions are known, no calibration is necessary, However, for convenience, the instrument is calibrated with particles or droplets of known size and, once tuned, the instrument does not require recalibration for different particles.

14.2.3.3 Precision and Accuracy The basic principle applied in the ESPART analyzer can provide absolute measurements of particle size and electric charge if the physical parameters involved in the experimental setup and in the ambient conditions are accurately known. For example, aerodynamic diameter depends upon the viscosity of the gas in which the particles are suspended. Since viscosity is independent of pressure over a wide range, the size measurement can be performed at different ambient pressures. However, if there is a significant change in temperature or in the constituents of the gas, the ESPART will measure the aerodynamic diameter related to the ambient viscosity of the gas in which the particles are suspended. This is an advantage of the ESPART analyzer for *in situ* measurements. A recalibration will be necessary when the ambient conditions or the instrumental parameters are different with respect to the previous calibration.

Precision of the ESPART measurements depends upon the minimization of the changes and drifts in the instrumental parameters such as LDV optical geometry, the frequency bias used in the LDV, the performance of the signal-processing circuitry and ambient conditions that affect the phase lag or amplitude ratio. The design parameters of the ESPART analyzer and the ambient conditions can be characterized during the testing and evaluation phase of the instrument. If there is any instrumental phase lag introduced by the signal-processing circuit, an appropriate offset value is used in the software for real-time correction. The phase offset value is determined during the calibration of the instrument with particles of known size.

When the instrument is operated at a relatively high acoustic frequency (>20 kHz), it is important to maintain a constant temperature inside the relaxation cell so that the phase offset value does not change. This constraint is less significant when the acoustic drive in the ESPART is in the lower range, or only an AC excitation is used.

Accuracy of measurement depends strongly upon the signal-to-noise ratio of the Doppler signal, the residence time of the particles in the sensing volume, and on the performance of the signal processing and data acquisition systems.

14.2.3.4 Frequency of Excitation: Resolution and Particle Count Rate The ESPART analyzer has been operated in a range 0.3–75 μm in aerodynamic diameter using two different frequencies of excitation. To cover this size range, it was necessary to operate the analyzer alternately, switching between two different frequencies of excitation, 20 kHz and 0.5 kHz, after every 5 min while sampling the aerosol stream for 20 min.

Figure 14-2 shows the dependence of the particle phase lag and the frequency of the acoustic or electric drive on the aerodynamic diameter. The frequency of the excitation field (acoustic or electric) is chosen depending upon the range of particle size for which the instrument is to be used. For example, for measuring particle diameters in the range 1 to 20 μm (for characterizing toner used in copying machines and laser printers), the drive frequency of choice is 2.0 kHz. For measuring particle size and charge distributions of therapeutic aerosols used for respiratory drug delivery in the aerodynamic diameter range from 0.5–10 μm, the instrument was operated at 20.0 kHz. Operating the instrument at the following four frequencies may provide a wide size range of operation: (1) $10.0 < d_a < 100.0$ μm in diameters: frequency 500 Hz; (2) $1.0 < d_a < 20.0$ μm: frequency 2.0 kHz; (3) $0.5 < d_a < 10.0$ μm: frequency 20 kHz; and (4) $0.05 < d_a < 1.0$ μm: frequency 40 kHz. Selection of the operating frequency depends upon the desired resolution in the measurement of particle size as discussed below.

As shown in Figure 14-2, the variation of phase shift with respect to aerodynamic diameter, $d\phi/d(d_a)$, depends upon the frequency of operation. To obtain the highest size resolution $d\phi/d(d_a)$ should be maximum, which occurs when the phase lag $\phi = 30^\circ$ or $\omega\tau_p = 1/\sqrt{3}$ (Mazumder et al. 1979). For accurate measurements of particle size and charge, it is desired to have a residence time of individual particle in the sensing volume for a period of at least two cycles of the driving excitation. For example, if the frequency of excitation is 2.0 kHz, each particle should have a transit time in the sensing volume for a minimum period of two cycles, that is, 1.0 ms. An approximate 1.0-ms time period is needed for the software to compute particle size and charge. Therefore, in this case, each particle count will require 2.0 ms for processing. The maximum count rate will be limited to less than 500 counts per second when the signal-to-noise ratio of the Doppler signal is high. At an excitation

frequency higher than 2.0 kHz, the maximum count rate depends upon the minimum time required by signal and data-processing circuitry for real-time size and charge analyses.

14.2.3.5 Range of Electrostatic Charge Measurements The ESPART analyzer can measure electrostatic charge on each particle in the range from zero charge to its saturation value with positive or negative polarity. The maximum or saturation charge on each particle is limited by the breakdown electric field of the surrounding medium created by the charge on the surface of the particle. For example, the breakdown electric field (E_{BD}) in dry air is 3.0×10^6 V/m.

The saturation charge-to-mass ratio of dielectric solid particles varies inversely with particle diameter. The experimental data on q/m versus diameter show this relationship consistently for toner charged against carrier beads. The minimum charge that can be measured on a particle depends upon the sensitivity of the amplitude ratio measurements. The accuracy of charge measurements depends upon the number of cycles during which charge measurements are made. Using 0.8-μm diameter PLS spheres and eight cycles of residence time, ESPART measurements could resolve charge by 2 electronic charges as measured against an electrical mobility analyzer (Mazumder et al. 1991).

14.2.3.6 Measurement of Particle Mass For each particle, the aerodynamic diameter (d_a) and the charge (q) are determined by the ESPART analyzer and the average value of the charge-to-mass ratio (q/m) computed. For a spherical particle of diameter d_p and specific gravity ρ_p, we can write an approximate relationship:

$$d_p^2 \rho_p = d_a^2 \rho_o \qquad \text{(Eq. 14-28)}$$

The mass m_p of the particle can be computed from the measured value of d_a, if the actual particle density, ρ_p, is known, by using the equation

$$m_p = \pi \rho_o^{3/2} d_a^3 / (6\rho_p^{1/2}) \qquad \text{(Eq. 14-29)}$$

For each size channel $(d_a)_i$, from $i = 1$ to $i = 32$, the particle count is stored as n_i; m_p for each channel is approximately $\pi n_i \rho_o^{3/2} d_a^3/(6\rho_p^{1/2})$. The total mass of the particle sample is given by summing over i channels:

$$m = \sum (m_p)_i = \frac{\pi \rho_o^{3/2}}{6\rho_p^{1/2}} \sum n_i (d_a)_i^3, \qquad \text{(Eq. 14-30)}$$

for each size channel, $(d_a)_i$, the total count n_i is also stored in the charge channels. The sums are performed over all 32 channels. The total number of particles, n_i, is equal to $n^o + n_i^+ + n_i^-$, where n^o, n_i^+, and n_i^- represent the total number of particles with zero, positive, and negative charges respectively with diameter $(d_a)_i$, respectively. The software performs the computations and plots of n_i^+, n^o, n_i^-, versus charge-to-mass (q/m) ratio for all channels $(d_a)_{I-n}$. The analyzer provides q/m ratio for positively and negatively charged particles along with the number and total mass of the particles having positive and negative charges. The net average charge-to-mass $(q/m)_{net}$ ratio of all the particles sampled is also provided. A three-dimensional plot of number of particles versus charge-to-mass ratio and d_a is also available.

14.2.4 Measurements Under Different Atmospheric Conditions: Applications to Mars and Measurements of Nanoparticles

ESPART analyzer is capable of measuring particle size and charge distributions in different atmospheric conditions. Relaxation time τ_p is determined by determining the atmospheric parameters involved using Equation 14-5, $\tau_p = (\rho_p d_p^2/18\eta)C_c$.

One instrument was developed for its possible application in the Martian atmosphere (Srirama et al. 2007). Ambient conditions on the surface of Mars are: average temperature: 227 K; primary component of the atmospheric gas: CO_2; particle density of Mars dust: 2500 kg/m^3; and the ambient pressure range: 5–10 mb. Based on these ambient conditions, $\eta = 1.147 \times 10^{-5}$ Pa · s. As shown earlier, the phase lag is related to the frequency of excitation and the relaxation time, given by $\phi = \tan^{-1} \omega\tau_p$.

Figure 14-9 shows a plot of the phase lag versus aerodynamic diameter using an excitation frequency of 2.0 kHz under the Martian atmospheric conditions (Srirama et al. 2007; Sharma et al. 2008). The phase-shift relationship is significantly different under the earth's and Martian atmospheric conditions. It is interesting to note that the phase lag is much larger at a low pressure (7 mb) compared to the atmospheric pressure of Earth (1013 mb).

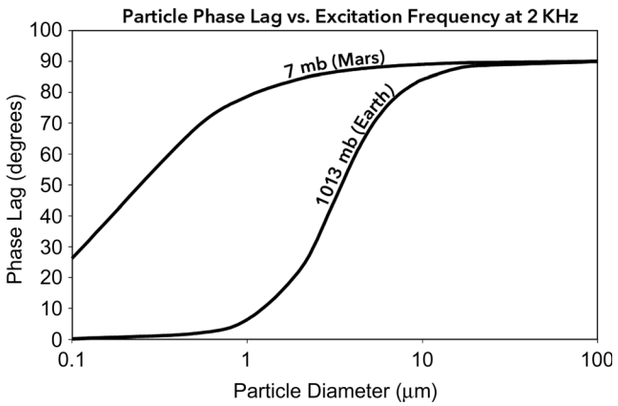

Figure 14-9 Phase lag variation as a function of particle diameter and at an excitation frequency of 2 kHz on Mars (7 mb) and Earth at normal pressure (1013 mb).

The higher phase lag values for small particles at a relatively low frequency of acoustic or electric drive would allow measurement of size and charge distributions of nanoparticles with much higher accuracy. Under earth's atmospheric condition, characterization of nanoparticles can be performed within an evacuated chamber at a low pressure of 10 mb. The higher phase lag values for small particles at a relatively low frequency of acoustic or electric drive would allow measurement of size and charge of small particles with much higher accuracy compared to measurements that can be performed under normal atmospheric pressure conditions.

14.3 AERODYNAMIC PARTICLE SIZER

14.3.1 Measurement Principles

The Aerodynamic Particle Sizer (APS) sizes a particle by measuring its velocity relative to the air velocity within an accelerating airflow. The accelerating flow field is produced by passing an aerosol through a nozzle. The gas velocity U_g in the nozzle can be calculated from the Bernoulli equation for compressible flow

$$U_g = \left[\frac{2RT}{M}\ln\left(\frac{P}{P-\Delta P}\right)\right]^{1/2} \qquad \text{(Eq. 14-31)}$$

where R is the universal gas constant, T is the absolute temperature, M is the gas molecular weight, P is the ambient pressure and ΔP is the pressure drop across the nozzle. The velocity of a particle V_p can be determined from

$$V_p = \frac{U_g\, t_{min}}{t} \qquad \text{(Eq. 14-32)}$$

where t is the transit time of the particle [referred to as the time-of-flight (TOF)] and t_{min} is the minimum transit time for small particles at a fixed distance downstream of the nozzle. Time-of-flight is measured as the time between two pulses of light scattered by the particle as it passes through two beams of light. For a progressively larger particle, TOF becomes longer because the particle lags behind the air velocity to a greater extent. The TOF data are stored in an accumulator in bins representing time intervals. A calibration curve relates particle size with the accumulator TOF spectrum. This curve is based on the fact that the ratio of V_p/U_g as a function of Stokes number is unique for a given acceleration nozzle and light detection arrangement.

Particle number concentration by size is derived directly from the accumulator bin data. However, the particle velocity is a function of aerodynamic diameter d_a for laminar flow (within the Stokes regime, $Re_p < 0.1$) only. As Re_p becomes greater (non-Stokesian), the apparent particle size becomes a function of particle density and shape in addition to aerodynamic diameter. At greater nozzle velocities, particle motion becomes more non-Stokesian (less accurate aerodynamic sizing) but smaller particles may be detected and sizing is more rapid. Artifacts in the observed aerodynamic distribution may occur because the light scattering used for detection of particles results in incomplete detection or particle coincidence. Liquid droplets may be undersized because they flatten and achieve greater velocities than spherical solid particles in the accelerating flow field.

14.3.2 Aerodynamic Particle Sizer Models

14.3.2.1 Standard Time-of-Flight Aerodynamic Particle Sizer The design of the APS is based on the design of a particle acceleration nozzle and laser Doppler detection system constructed by Wilson and Liu (1980). ***TSI*** has offered several APS models over the past three decades (the first three models are now discontinued):

- Model 3300—Based on prototype design; used an Apple II computer for data analysis; HeNe laser light source; valve control monitored with mass flow meters (Agarwal and Ramiarz 1981).
- Model 3310—Updated to IBM PC-compatible computer for data analysis; advanced software size spectrum analysis package available (Blackford et al. 1988).
- Model 3320—Updated detector optics (double-crest signal) and signal-processing circuitry with a solid-state laser diode; redesigned smaller overall package with integrated particle spectrum readout and microprocessor-controlled volumetric flow; provided lower size resolution but better coincidence rejection than 3310; light-scattering intensity data available (Caldow et al. 1997; Stein et al. 2002).
- Model 3321—Redesigned aerosol exit nozzle from the detector region (Stein et al. 2003).

All models use the same flow path to deliver an aerosol to the detector region (Fig. 14-10). Aerosol is introduced to the inlet at a flow rate of 5 L/min. Of this flow, 4 L/min is removed, passed through a filter, and re-introduced upstream of the acceleration nozzle as sheath flow. The remaining 1 L/min aerosol flow traverses the inner tube, is accelerated by the inner, or focusing, nozzle (60° angle with the direction of flow), and then recombined with the cleaned, particle-free sheath flow. The combined aerosol and sheath flow then pass through the final outer acceleration nozzle into the detector region. The air velocity reaches approximately 150 m/s at the exit of the acceleration nozzle.

Flow control in the newer APS Models 3321 and 3320 is substantially improved over earlier models. In earlier models, a decrease in pressure at the inlet decreases the airflow

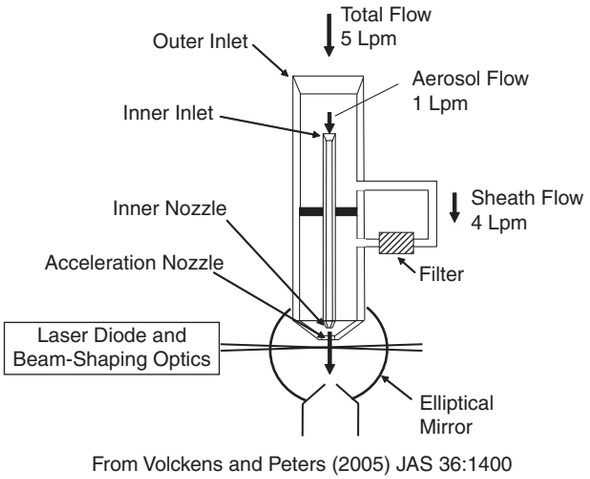

Figure 14-10 Schematic diagram of the Aerodynamic Particle Sizer (Models 3320 and 3321).

through the acceleration nozzle and shifts the calibration curve to larger sizes. This effect was especially problematical for submicrometer particles that are especially sensitive to slight changes in the calibration. This problem is especially apparent when comparing size distributions upstream and downstream of a classifier (e.g., cyclone or impactor) that impart a pressure drop on the APS inlet. The improved flow control in the newer models includes a second pump that helps regulate the sheath flow and reduces the likelihood of calibration shift with small inlet pressure changes.

Detection of particle TOF has changed in newer APS models. In Models 3321 and 3320, illumination of the particle downstream of the acceleration nozzle results in two overlapping pulses of light, referred to as a double-crest signal (Fig. 14-11a). The pulse shape is differentiated, and the inflection point of each peak defines the center point or mode of that peak. The TOF is measured as the time between

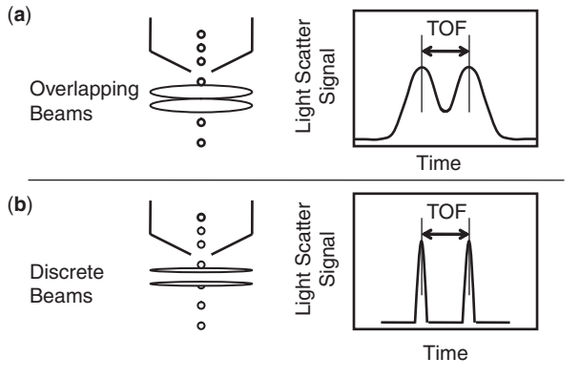

Figure 14-11 Schematic representation of light signals produced by a particle passing through the detection region of the APS: **(a)** Models 3320 and 3321; and **(b)** Models 3300 and 3310.

the modes of the each pulse. The APS also records scattered-light intensity that may be recorded as a separate spectrum or correlated with each TOF measurement. The way the signal is processed facilitates detection of particle coincidence—the presence of more than one particle in the detection region simultaneously—and is reviewed in Section 14.3.2.4.

In older models (APS 3300 and 3310), the particle produces two discrete signals as it passes through two sharply focused beams 200–500 μm downstream of the acceleration nozzle (Fig. 14-11b). This arrangement is subject to numerous and complicated coincidence issues (Heitbrink and Baron 1991), although it potentially yields better sizing resolution compared to that in newer models. The reader is referred to Heitbrink and Baron (1991) for a thorough discussion of signal processing in older APS models. Erroneous "phantom counts" (large particles clearly not present in the aerosol but found in size spectrums with $d_a > 10$ μm) were once solely attributed to particle coincidence.

The modified exit flow path introduced with the APS Model 3321 resolved a key issue of recirculating particles that do not properly exit the older APS models (Peters and Leith 2003; Reid and Peters 2007). These recirculating particles can become entrained back into the aerosol flow path and enter the detection region. They are not properly accelerated because they do not pass through the acceleration nozzle and are consequently oversized ($d_a > 10$ μm). Stein et al. (2002) called these particles "anomalous" to distinguish their source as distinct from phantom counts produced by coincidence. The relative magnitude of the role that coincidence and recirculation plays in creation of spurious counts in the size spectrum with $d_a > 10$ μm for APS Models 3300 and 3310 is unclear.

14.3.2.2 Ultraviolet Aerodynamic Particle Sizer A ultraviolet Aerodynamic Particle Sizer (TSI; UV-APS), also referred to as fluorescence APS or FLAPS is designed specifically to detect biological aerosols. The currently available Model 3314 UV-APS measures the fluorescence intensity of individual airborne particles in addition to their aerodynamic diameter and scattered-light intensity. It uses the same flow path and double-crest optical system found in the Model 3321 APS. Particle fluorescence is excited by a pulsed-ultraviolet laser and is collected real time using a photomultiplier tube. The Model 3312 UV-APS is an earlier version that is based on the Model 3320 APS.

14.3.2.3 Time-of-Flight Calibration A calibration curve relates particle TOF to aerodynamic diameter. This curve is typically developed using aerosols composed of monodisperse latex spheres. Aerosol with spheres <5 μm can readily be generated by nebulizing a water suspension of the spheres. Although isopropyl alcohol suspensions of latex spheres may be easier to generate and dry than water, the alcohol can slowly dissolve latex spheres and cause them to swell to a

larger size. Larger calibration particles can be generated dry from a surface by suction, as with the Small Scale Powder Disperser (Model 3433, ***TSI***), or by gently brushing the spheres from a clean surface, such as a glass slide. Other monodisperse particles, such as those generated from the vibrating orifice monodisperse aerosol generator (VOMAG, ***TSI***), can also be used for calibration. However, oil droplets distort into oblate spheroids due to the high acceleration (see Section 14.3.3.2) and exhibit a smaller aerodynamic diameter than that for a sphere (Baron 1986). Thus, only solid particles should be used to calibrate the APS, unless it is to be used with the particular liquid for which the calibration is performed.

A complete calibration curve is obtained by fitting a spline or polynomial function to the discrete calibration points obtained with multiple monodisperse aerosols. This curve is dependent on the particle velocity, which is affected by the distance of the laser beams from the acceleration nozzle. In newer APS Models 3321 and 3320 the distance of the laser beam from the nozzle and beam spacing is more tightly controlled during manufacture and can be reset without extensive recalibration. The sensor region is thus more accurately positioned and the calibration from instrument to instrument should be more consistent. In older APS Models 3300 and 3310, these nozzle sizes, spacing, and laser beam locations were more difficult to control, resulting in a unique calibration for each instrument.

Once the calibration of the APS has been completed in air at ambient pressure, calibration for other gas viscosities and pressures can be achieved as described by Rader et al. (1990). Tsai et al. (2004) propose a universal calibration curve for accurate determination of particle aerodynamic diameter at various temperatures, pressures, and particle and gas properties. The procedure that they outline for calibration accounts for non-Stokesian particle-sizing issues discussed Section 14.3.3.1.

14.3.2.4 Particle Counting Efficiency The APS must correctly count and size particles to accurately measure the particle size distribution. Sizing accuracy is addressed in subsequent sections. The overall counting efficiency of the APS is a product of sample aspiration η_a, transmission η_t, and detection efficiency η_d

$$\eta_{overall} = \eta_a \eta_t \eta_d \qquad \text{(Eq. 14-33)}$$

Aspiration and transmission of aerosol through the acceleration nozzle are similar for different APS models because the nozzle geometries and flow rates have not changed. Transmission of small particles by recirculation was reduced with the introduction of the Model 3321. Detection algorithms have changed as new optics and signal-processing circuitries have been introduced in new models.

14.3.2.5 Aspiration Sampling an aerosol with the APS involves aspiration into the instrument (outer inlet) and into the inner nozzle (Fig. 14-10). Aspiration into the 2-cm-diameter outer inlet is affected by factors external to the instrument, such as windspeed and direction (Chen et al. 1998). The position of the outer inlet at the top of the instrument commonly requires an aerosol to be ducted to the APS with external tubing. Particle losses in such tubing and bias introduced by non-isokinetic sampling of moving airflows may be accounted for with the approach outlined in Chapter 7 of this book.

Only 20% of the aerosol enters the inner inlet and is measured. Consequently, special attention may be required to produce a well-mixed aerosol in this region when components upstream of the APS (e.g., bends in tubing or cyclones) may impart nonuniformities in particle concentration. The gas velocity at the measured flow inlet is higher than the velocity at the APS inlet, that is, superisokinetic (Kinney and Pui 1995). This sampling arrangement produces some oversampling of larger particles to compensate for losses within the inner nozzle tube. Calibration curves have been developed by the manufacturer and are provided as part of the computer software to compensate for sampling losses at this point.

A sample dilutor system is commercially available as optional equipment for the APS (Model 3022A, ***TSI***). Within the APS software, a user may apply a manufacturer-provided penetration curve to correct a measured size distribution for particle losses that occur within the dilutor. However, particle losses are near 50% at 15 μm and increases rapidly with increasing d_a. Corrections of this magnitude introduce substantial uncertainty of the data in the largest size channels of the APS.

14.3.2.6 Transmission As shown in Figure 14-12, liquid droplets may impact and collect in the inner nozzle, whereas most solid particles bounce through the system and are detected with near 100% overall counting efficiency (Volckens and Peters 2005). These observations suggest that solid particles bounce off the surfaces of the inner nozzle and re-entrain into the airflow. For 10-μm monodisperse oleic acid droplets, Volckens and Peters (2005) found 3% deposited in the inner inlet, 4% deposited within the inner tube, 41% deposited at the tip of the inner nozzle, and 26% were counted correctly by the detector. However, they were unable to account for all of the droplets and suggested that further losses may occur on the final acceleration nozzle. Similar results have been obtained using a computational fluid dynamics (CFD) model (Baron et al. 2008). Use of an inlet with a smaller nozzle angle (2° or 8°) has been shown to reduce losses in the inner nozzle but also reduces the resolution of the APS (Kinney and Pui 1995).

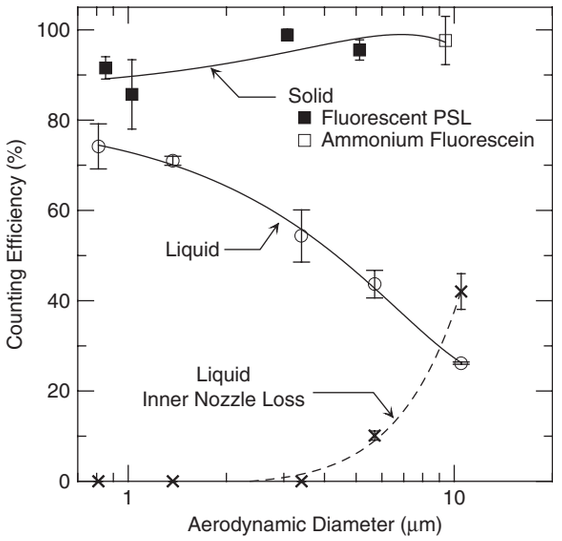

Figure 14-12 Counting efficiency of the APS 3321 and liquid losses within the inner nozzle versus aerodynamic particle diameter. Reprinted from Volckens and Peters (2005) with permission.

14.3.2.7 Detection In newer models (APS 3320 and 3331), a laser diode illuminates the particle with two relatively broad beams of visible light (680 nm), resulting in two overlapping pulses of light detected with a solid-state avalanche photodetector (Fig. 14-11a). The resulting continuous signal is used to sort the particle into one of four events (Fig. 14-13):

Type 1: a small particle produces only one signal crest above threshold and data is logged for concentration calculations in the <0.5-μm accumulator channel;

Type 2: a valid particle measurement when two signal crests above threshold and TOF is logged for concentration calculations in the appropriate accumulator channel;

Type 3: multiple particles coincident in the detector region that produce three signal crests above threshold and the event is logged but not used to calculate concentration; and

Type 4: a recirculating particle produces two signal crests above threshold but TOF >4.096 μs and event is logged but not used to calculate concentration.

The newer detection circuitry facilitates identification of coincident particles in the sensor region. Coincidence may still bias the measured particle size distribution because coincident particles are not logged in the TOF data. However, the number of Type 3 events relative to the number of valid Type 2 counts provides an estimate of the importance of coincidence events. Further research is needed to allow a quantitative estimate of the change in the measured size distribution due to particle coincidence.

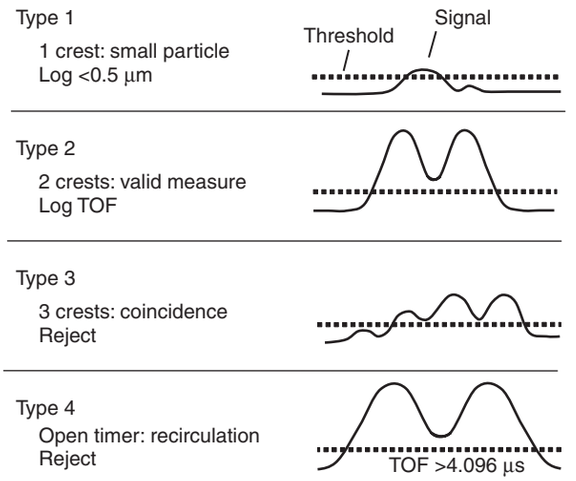

Figure 14-13 Signal processing in the APS (Models 3320 and 3321).

The light scattered by the particle is also available as a separate spectrum or correlated with TOF data. Although scattering is a function of particle refractive index and shape, these data have proven very useful in development of the APS. Stein et al. (2002) used correlated information from an APS 3320 to identify particles with a light-scattering intensity that was too low given their measured aerodynamic diameter (Fig. 14-14). Using CFD modeling, Stein and coworkers attributed these observations to particles that did not exit the detector region properly, were recirculated back

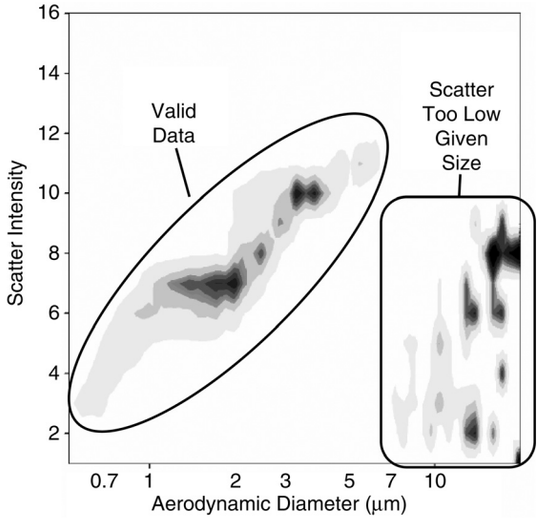

Figure 14-14 Light-scattering intensity versus aerodynamic diameter measured with an APS Model 3320. Reprinted from Stein et al. (2002) with permission.

into the sensor region, and were sized too large because they were not subject to the full acceleration forces in the inner nozzle. This work led to a redesign of the exit nozzle with the introduction of the APS 3321 that appears to have substantially reduced or eliminated recirculation (Peters and Leith 2003; Stein et al. 2003).

14.3.2.8 Overall Counting Efficiency As indicated in Figure 14-12, the overall counting efficiency of the APS Model 3321 ranges from 85% to 99% for solid particles, whereas that for liquid droplets progressively decreases from 74% at 0.8 μm to 26% at 10 μm (Volckens and Peters 2005; Baron et al. 2008). For concentrations at which coincidence should be minimal, Volckens and Peters (2005) measured similar overall counting efficiency among APS Models 3321 and 3310 for solid monodisperse latex spheres. Agreement among mass distributions measured with a cascade impactor and an APS Model 3321 (Stein et al. 2003) supports the finding of near 100% overall counting efficiency for solid aerosols.

14.3.3 Particle Sizing Issues

14.3.3.1 Non-Stokesian Corrections The acceleration in the nozzle produces particle Reynolds numbers that are outside the Stokes regime, as indicated in Table 14-1. Thus, the measured size is dependent on other factors besides the aerodynamic diameter, including gas density, gas viscosity, particle density, and particle shape (Wang and John 1987; Ananth and Wilson 1988). The true aerodynamic diameter of a particle may be estimated if these factors are known by iterating the following equations (Rader et al. 1990).

$$\sqrt{Stk_2} = \sqrt{Stk_1}\left(\frac{6 + R_2^{2/3}}{6 + R_1^{2/3}}\right)^{1/2} \qquad \text{(Eq. 14-34)}$$

$$R_1 = \xi_i^{3/2}\sqrt{Stk_i}\,|U_g - V_p| \qquad \text{(Eq. 14-35)}$$

TABLE 14-1 Particle Properties in the APS Nozzle

Particle Diameter (μm)	Relative Velocity (cm/s)	Particle Reynolds Number	Weber Number (oil droplets)[a]
0.5	40	0.013	2.9×10^{-6}
1.0	1750	1.16	0.0113
3.0	6490	12.9	0.468
10.0	10,600	69.6	4.13
15.0	11,500	114.0	7.36
20.0	12,300	163.0	11.2

Reprinted from Baron (1986) with permission.
[a]These represent either oleic acid or di-octyl phthalate, both of which have a surface tension of about 0.033 N/m [33 dyne/cm].

$$\xi_i = \left(\frac{18\,\rho_{gi}^2\,S}{\rho_{pi}\,\mu_i\,U_g}\right)^{1/3} \qquad \text{(Eq. 14-36)}$$

where subscript 1 refers to calibration conditions with unit density spheres, subscript 2 refers to measurement conditions, *Stk* is the Stokes number, and S ($= U_g\,t_{min}$) is the distance between the laser beams. Measurements were made in argon and N_2O to confirm that this approach improved the accuracy of aerodynamic size measurement (Lee et al. 1990; Rader et al. 1990). The slip correction factor must also be modified in the above equation because of the reduced pressure in the nozzle. Computer code included in the APS software as the "Stokes Correction" algorithm is available to perform these corrections (Wang and John 1989).

Nonspherical particles may be undersized due to non-Stokesian particle movement. Cheng et al. (1990) included particle dynamic shape factor in the above iterative correction procedure to account for this effect. However, this approach may be inadequate for extreme shapes such as fibers.

The APS has been shown to provide the same aerodynamic diameter for fibers of identical diameter but different length. Fibers and other nonspherical particles tend to orient themselves with their maximum cross section oriented perpendicular to the flow (Clift et al. 1978). However, larger fibers (on the order of 10-μm diameter) may not have sufficient time to orient in the flow field and may produce a measured size intermediate between the perpendicular and parallel orientation. Thus, the initial conditions of the particle (e.g., orientation, location in the flow field) during acceleration can affect the measured aerodynamic size.

14.3.3.2 Issues with Sizing Droplet During acceleration, droplets distort into oblate spheroids with the maximum cross section perpendicular to the direction of motion, increasing the drag and causing them to be undersized (Fig. 14-15). The distortion of a droplet in the sensing zone depends on droplet size, the liquid surface tension, and viscosity. The Weber number, $We = u^2\rho d_p/\gamma$, where u is the particle velocity relative to the air and γ is the droplet surface tension, represents the ratio of the air pressure force to the surface tension force. Droplets will eventually break up when experiencing Weber numbers between 12 and 20. Distortion increases with droplet size because the force on the droplet increases with size. While the Weber number indicates the maximum distortion that the droplet can undergo, the droplet viscosity determines the rate at which the droplet distorts. The rapid acceleration in the APS nozzle usually precludes droplet breakup prior to reaching the sensing zone. Since the acceleration is high, viscosity is the controlling factor for distortion of many liquids (Griffiths et al. 1986).

The degree of distortion has been calculated and agrees well with experimental measurements of the droplet undersizing for several oils with different viscosities (Bartley

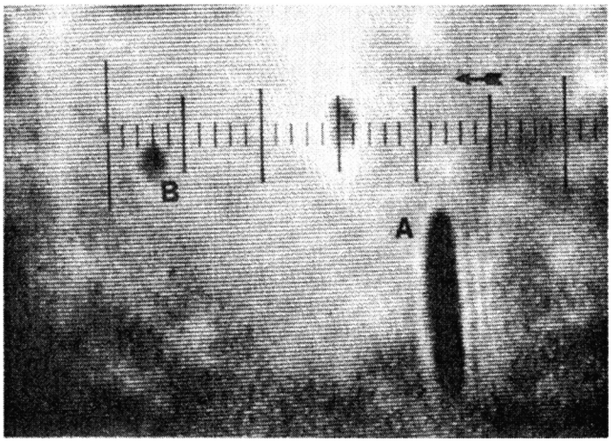

Figure 14-15 Picture of droplets in the high velocity air jet just beyond the APS nozzle taken with a high-speed laser-imaging system showing a droplet flattened by the drag force. The nozzle tip is about 200 μm to the right of droplet A with the air and the droplets moving to the left. The scale markers are approximately 5 μm apart. The larger droplet A has an extreme 10-by-60 μm spheroidal shape while the smaller droplet B is about 8 by 10 μm and is only slightly flattened.

et al. 2000; Baron et al. 2008). Water droplets, which have a low viscosity but relatively high surface tension, distort less in the acceleration field (Baron 1986; Bartley et al. 2000). In addition, the degree of distortion is dependent on the precise acceleration history and therefore can vary from instrument to instrument. Baron et al. (2008) expressed the size shift—the difference in the actual and the APS-measured droplet diameter—as the empirical function

$$\Delta = -\frac{(2.723 \times 10^{-4})d^2}{\eta^{0.6486}\gamma^{0.3864}} \qquad \text{(Eq. 14-37)}$$

As shown in Figure 14-16, this function fit experimental data well for a wide range of viscosities, although it has only been validated for a narrow range of surface tension. Table 14-2 presents the surface tensions and viscosities associated with the oils displayed in this figure.

Liquid accumulated at the tip of the inner nozzle can constrict the nozzle, increase the velocity in the sensing region, and further shift the APS-measured diameter to smaller sizes (Baron et al. 2008). Baron et al. (2008) measured this shift to be smaller with a clean inner nozzle than with an inner nozzle loaded with liquid. Further, they found that this shift can occur in only 1–10 minutes at relatively low concentration (1000 particles/L) after deposition of <0.5 μL liquid and can disappear after cessation of liquid aerosol sampling. Equation 14-37 applies best for a nozzle after this initial loading time period.

14.3.4 Applications

The APS has been used to measure particle size distributions in a variety of applications. Good correlation of the APS with cascade impactor measurements for solid particles has led to its use in measuring laboratory (Peters et al. 1993) and pharmaceutical aerosols (Stein et al. 2003). An APS combined with an electrical sizing instrument (see Chapter 18) has been used to measure ambient size distributions

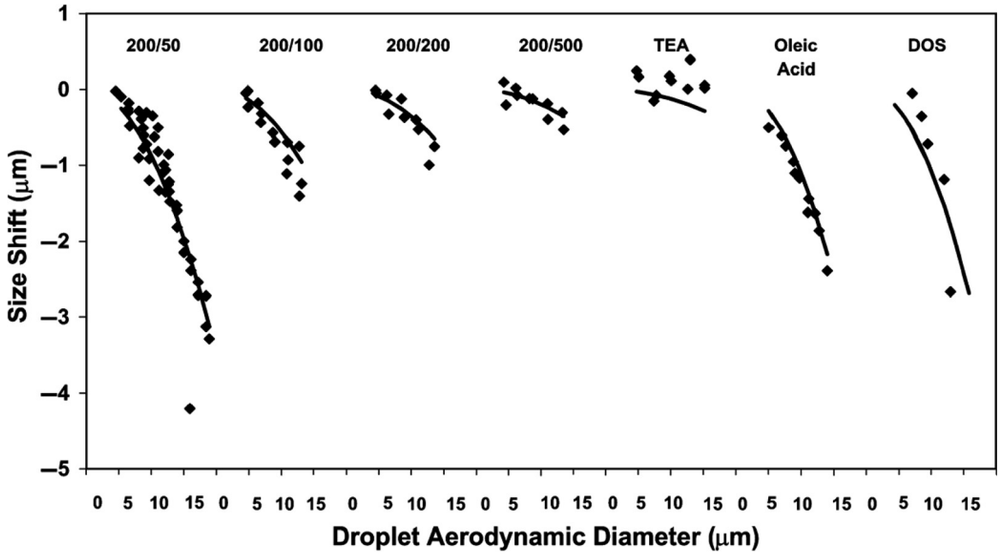

Figure 14-16 Size shift data for the APS along with the least-squares fit using Equation 14-31. Surface tensions and viscosities of different oils are provided in Table 14-1. The largest size shift value for Dow 200/50 was treated as an outlier. Reprinted from Baron et al. (2008) with permission.

TABLE 14-2 Properties of Liquids Used in the Study of Droplet Size Shifts[a]

Oil Type	Surface Tension (N/m)	Viscosity (Pa · s)
200/50[b]	0.0208	0.048
200/100[b]	0.0209	0.0964
200/200[b]	0.021	0.1934
200/500[b]	0.0211	0.4845
Triethanolamine (TEA)	0.0489	0.59
Oleic acid	0.032	0.0256
Di-octyl sebacate (DOS)[c]	0.0322	0.027

[a]See Figure 14-16.
[b]Designation for Dow Corning polydimethylsiloxane oils.
[c]Also called (bis)-2-ethyl hexyl sebacate.

from 0.02–30 μm (Sioutas et al. 1999). The difference in measurement principles among these types of instruments may be used to estimate aerosol particle density and shape factor (Chen et al. 1990; DeCarlo et al. 2004; Stanier et al. 2004). The APS has been used to measure the size distribution of ambient coarse particles (Reid et al. 2003). Estimates of coarse particle mass concentration derived from the APS have been shown to correlate favorably with those made with reference samplers in some situations (Peters 2006).

The APS has been used for bioaerosol measurement (Baron and Willeke 1986). Specific detection of biologically based particles has been enhanced using the UV-APS Model 3314, where the fluorescence signal can be combined with the aerodynamic size to obtain characteristic size distributions of bioaerosols (Kanaani et al. 2008). The fluorescence intensity measured with the UV-APS has been shown to be linear for one type of bacterial cell up to a certain airborne concentration (Agranovski and Ristovski 2005). Different organisms demonstrate considerable differences in their fluorescence, potentially complicating interpretation of data from this instrument (Brosseau et al. 2000).

The APS has also been applied extensively to measure penetration curves of several types of aerodynamic classification devices, such as impactors (Jones et al. 1983; Misra et al. 2002; Lee et al. 2006), cyclones (Kenny and Gussman 1997; Chen et al. 1999; Maynard 1999), inlets (Kenny et al. 2004), and open-pore foams (Lee et al. 2005).

14.3.5 Aerodynamic Particle Sizer Performance Synopsis

The APS nominally measures the aerodynamic diameter of airborne particles in the range of 0.5–20 μm (52 channels/geometric scale). It is the most commonly used real-time particle counting instrument that classifies particles by aerodynamic diameter. There are complex issues in sizing accuracy and internal losses at different size ranges. Particle sizing resolution at all sizes is good. Particle coincidence is a function of size and size distribution, increasing dramatically with size. The instrument indicates when coincidence may be a problem. As with any complex instrument, frequent size calibration provides additional confidence in the accuracy of the results (see Chapter 21).

Performance of the APS in different size ranges can be summarized as follows:

- 0.5–1 μm: Sizing resolution drops off for small particles because they are accelerated to a velocity similar to that of the carrying airflow. Counting efficiency may be reduced because small particles may scatter insufficient light to be detected depending on composition (e.g., black particles). Internal particle transmission losses are minimal.
- 1–5 μm: Sizing accuracy may be affected by particle density and particle shape factor (non-Stokesian effects). Although particle density and shape factor may offset one another, density greater than 1 will produce overestimated sizes (e.g., for 5-μm spherical particles with a density of 2 g/cm^3, size will be overestimated by about 8%). Counting efficiency is near 100% for solid particles, although somewhat lower for droplets. Internal particle transmission losses are minimal.
- 5–20 μm: Sizing accuracy is affected by non-Stokesian effects as above, increasing with particle size. Droplets may flatten and be undersized depending on the properties of the liquid droplet. Deposited liquid droplets may also constrict the acceleration nozzle and cause further undersizing. Solid particles may hit the bottom of the inner nozzle and bounce into the sensor region. This phenomenon probably has minimal effects on sizing and counting but does occur for up to 80% of the larger particles. Losses in this range make determining size distributions of aerosols of unknown composition questionable. However, making comparative measurements (e.g., determining impactor cutpoints in this size range) may be accomplished with care.

14.4 AEROSIZER

14.4.1 Principles of Measurement

The Aerosizer (***TSI***) is based on the acceleration of particles and TOF principles, although at higher particle acceleration than in either the ESPART and APS. The idea of accelerating particles in a sonic expansion flow and measuring the terminal velocity was first proposed and demonstrated in laboratory prototype instruments by Dahneke and co-workers (Dahneke 1973; Dahneke and Padliya 1977; Cheng and Dahneke 1979; Dahneke and Cheng 1979). The Aerosizer is the commercial product of this aerosol-beam research. Figure 14-17 depicts a schematic of the particle-detection section of the device. The aerosol enters the inner capillary

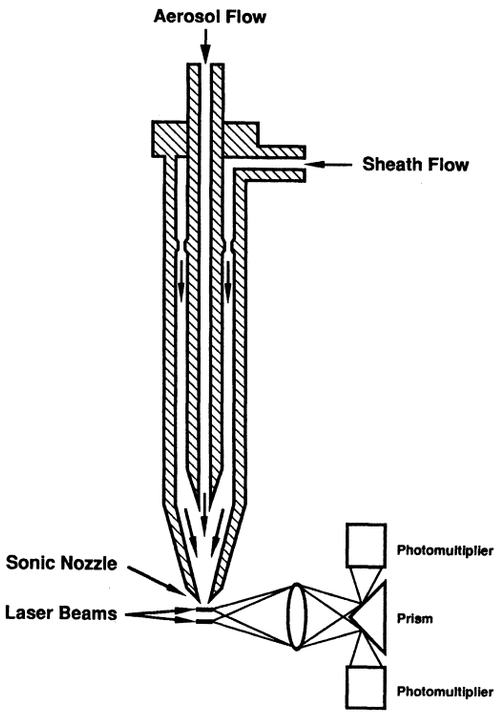

Figure 14-17 Schematic of the detection system of the Aerosizer. The two laser beams are perpendicular to both the aerosol flow and detection direction.

tube, surrounded by particle-free sheath air in the outer tube. Air and particles are accelerated through a convergent nozzle (0.75-mm diameter) with a 15° half angle and are delivered into a partially evacuated chamber. The ratio of pressure in the chamber and that in the ambient air is much smaller than 0.53; therefore, the air velocity at the nozzle exit, V_g, attains sonic velocity:

$$V_g = \sqrt{\frac{\gamma RT}{M}} \qquad \text{(Eq. 14-38)}$$

where γ is the ratio of specific heat capacities (1.4 for air); R is the gas constant; T is the temperature in K; and M is the molecular weight (28.96 for air). The air continues to expand in the chamber with a supersonic free-jet flow. The flow field in the convergent nozzle and the supersonic expansion have been described (Dahneke and Cheng 1979). From numerical calculations, it has been shown that the particle attains a terminal velocity soon after exiting the nozzle (Dahneke and Cheng 1979). At a distance of five nozzle diameters downstream of the nozzle, the calculated axial velocity is within about 2% of those at a distance of 50 diameters downstream.

The TOF of a particle is measured with two laser beams located close to the nozzle.

As particles pass through the laser beams, the light scattered from the particles is detected and converted into electronic signals by two photomultiplier (PMT) tubes. The distance between the two laser beams is about 1 mm with about a 20- to 30-μm spread of the individual beams. One PMT detects light as the particle passes through the first beam, while the other PMT detects the light from the second beam. The time between these two events (TOF) is measured and recorded to an accuracy of ± 25 ns. Each PMT converts the scattered light into an electrical pulse that is sent to the data-acquisition system. A low PMT threshold senses the weak pulses generated by small particles. However, at the low PMT threshold larger particles can cause the PMT to produce an electrical oscillation that generates multiple detected pulses from a single true pulse, a behavior called "ringing" (Thornburg et al. 1999). Therefore, the Aerosizer uses several PMT thresholds that are selected based on the initial pulse height so that spurious triggering on these subsequent oscillations does not occur.

Several models of the Aerosizer have been produced by Amherst Process Instruments, including the original Aerosizer, the Aerosizer LD and the Aerosizer DSP. Amherst Process Instruments was purchased by ***TSI*** in 1999 and the DSP version was designated Model 3220 (***TSI***). The principal improvements differentiating the models were: the Aerosizer LD had the HeNe laser replaced by a LD light source and the DSP model had an improved signal processor to reduce spurious triggering due to noise and ringing in large particle signals. Model 3220 has been discontinued and is not commercially available.

14.4.2 Calibration with Spherical Particles

The terminal velocity and TOF are functions of particle diameter, density, shape, and ambient pressure. Calibration curves (Fig.14-18) provided by the manufacturer are based on theoretical calculations and experimental data from solid spherical particles. The experimental validation of the calibration curves, also provided by the manufacturer, uses a limited number of monodisperse spherical particles of PSL and glass. A more extensive calibration of the instrument requires both PSL (density = 1050 kg/m^3 [1.05 g/cm^3]) and glass (density = 2460 kg/m^3 [2.46 g/cm^3]) particles with a size range of 0.5 to 150 μm obtained at an ambient pressure of 0.82 and 1 atm. This work is shown in Figure 14-19 (Cheng et al. 1993). Calibration curves for particles of these densities were calculated from the Aerosizer calibration table using an interpolation method and are plotted along with the measured data in Figure 14-19. Excellent agreement was found between the TOF of the PSL particles in the size range of 2–10 μm at 101.3 kPa [1 atm]. At a reduced pressure of 0.82 atm, the TOFs obtained for the PSL and glass particles were slightly higher than predicted by the calibration curves for the size range from 0.4 to 150 μm geometric diameter. However, the calibration tables were developed for normal ambient conditions, and theory predicts higher TOFs for operation under reduced ambient pressure (Dahneke and

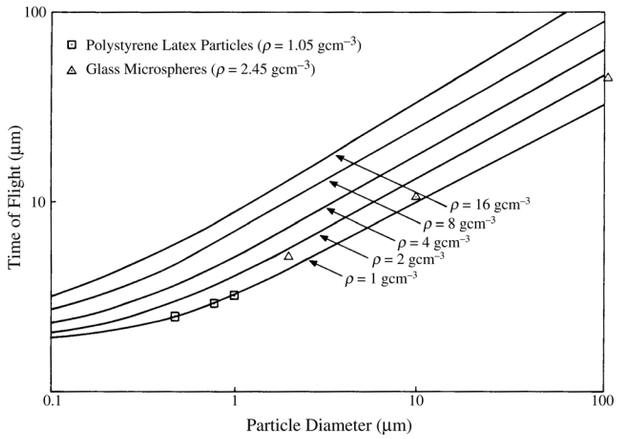

Figure 14-18 Calculated Aerosizer calibration curves for spherical particles of different densities. Reprinted from Cheng et al. (1993) with permission.

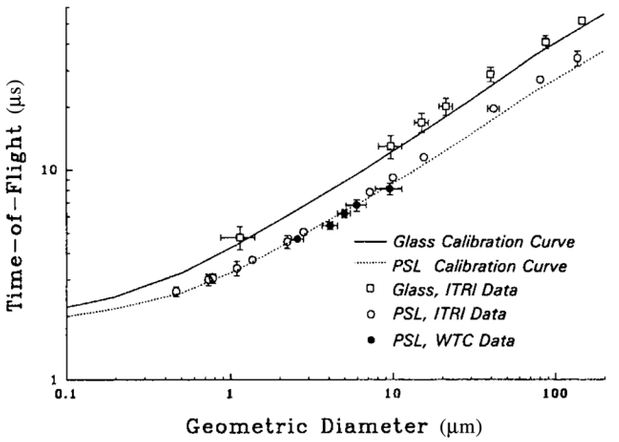

Figure 14-19 Aerosizer calibration data for latex particles (density = 1050 kg/m^3 [1.05 g/cm^3]) and glass beads (density = 2450 kg/m^3 [2.45 g/cm^3]). Reprinted from Cheng et al. (1993) with permission.

Cheng 1979; Oskouie et al. 1998; Tsai et al. 1998); thus, the disagreement between the measured data and calibration curves was expected. The magnitude of the overestimation of particle size by the Aerosizer is expressed in terms of the ratio of the geometric diameter measured by the Aerosizer to the true geometric diameter from microscopy (D_{API}/D_g). This ratio took values between 1.08 and 1.27 for the PSL particles and glass beads.

Tsai et al. (1998) calculated the particle trajectory assuming compressible flow in the Aerosizer nozzle, with a corresponding drag coefficient formula suitable for a range of Mach numbers and Reynolds numbers and appropriate for the Aerosizer operating conditions. The calculated TOF is in good agreement with experimental data obtained at 83.1 kPa [0.82 atm] pressure (Fig. 14-19). Compared to the calibration curve in Figure 14-18, the calculated results show deviation for particles greater than 10 μm. This deviation was due to the fact that Figure 14-18 was calculated assuming a one-dimensional flow field and a different formula for drag coefficient.

14.4.3 Instrument Responses with Nonspherical Particles and Droplets

Responses from the Aerosizer for nonspherical natrojarosite particles [Na $Fe_3(SO_4)_2$ $(OH)_6$] were measured (Cheng et al. 1993). Preparation and characterization of the uniform-sized particles formed as single, symmetrical truncated cubes with a density of 3.11 g/cm^3 have been described (Marshall et al. 1991). Particles having sizes between 7.3 to 18.8 μm aerodynamic diameter were prepared and classified by aerodynamic size in a Timbrell spectrometer. Figure 14-20 presents plots of the Aerosizer-measured aerodynamic diameter against mean aerodynamic diameter. In all cases, the Aerosizer significantly undersized the natrojarosite particles, and the degree of size reduction was size-dependent. Thus, the largest particles with true aerodynamic diameters close to 18.8 μm were undersized by as much as 51%, whereas the smallest particles analyzed with true aerodynamic diameters of 7.3 μm were undersized by only 21%.

Liquid droplets also behave differently than solid spherical particles in the Aerosizer. The Aerosizer underestimates the true aerodynamic diameter of oleic acid droplets (Tsai et al. 1998), similar to results shown by Baron (1986) and Bartley (2000) from the APS. The deformation is a function of the Weber number (Baron 1986; Lefebvre 1989). A

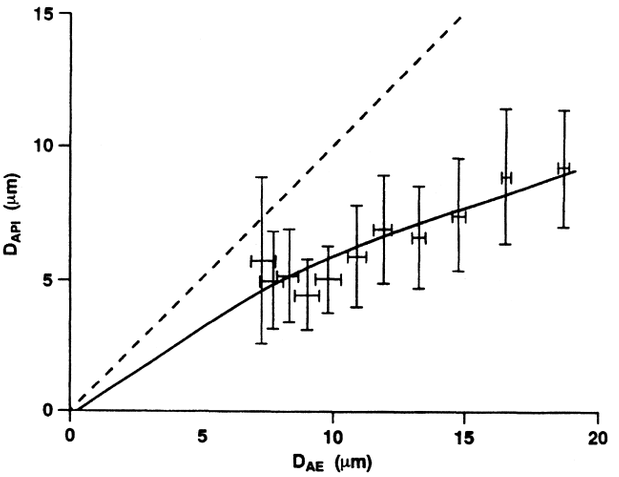

Figure 14-20 Comparison between the Timbrell Spectrometer and the Aerosizer-measured aerodynamic diameters of natrojarosite at normal ambient pressure (100 kPa [750 mm]). Reprinted from Cheng et al. (1993) with permission.

Weber number greater than the range of 12–20 suggests that the droplets broke up, whereas Weber numbers within that range indicate that the droplets may have deformed (Lefebvre 1989). Calculations of Weber numbers for 1- and 5-μm oleic acid showed that particles larger than 5 μm have Weber numbers in the 12–20 range and may deform in the measurement region (Thornburg et al. 1999). These results agree with experimental data showing particle deformation for oleic acid particles greater than 7 μm (Baron et al. 1996; Tsai et al. 1998). The Aerosizer is thus likely to exhibit a greater degree of droplet deformation than the APS due its higher particle acceleration.

14.4.4 Comparison Between the Aerosizer and the APS

Both the Aerosizer and the APS are based on the acceleration of particles in an aerosol beam and TOF measurement for size determination. However, the details of design and operation of these two instruments differ substantially. Whereas the APS is operated under subsonic flow with about 13.3 kPa [100 mm Hg] pressure differential between the ambient air and sensing volume (Chen et al. 1985), the Aerosizer is operated under supersonic conditions with a much higher pressure drop (greater than 100 kPa [750 torr] under 101.3 kPa [1 atm] ambient pressure). Therefore, a more powerful vacuum pump is needed for the Aerosizer, whereas the APS uses much smaller pumps placed inside the instrument. Because the nozzle in the Aerosizer is operated as a critical orifice, it controls the flow by itself. However, the APS requires a more elaborate flow-control system to keep a constant sampling flow rate. The Aerosizer has higher gas and particle velocities than the APS, for example, a 10-μm PSL particle attains about 100 m/s velocity in the Aerosizer versus about 38 m/s in the APS. With a higher velocity, and therefore a higher Reynolds number, in the Aerosizer, the drag force experienced by a particle will be higher than that in the Stokes regime ($Re < 0.1$). Therefore, the effects of particle density and shape factor on the instrument response will be greater in the Aerosizer than in the APS.

Another major difference between the Aerosizer and the APS is the method for measuring the TOF. The Aerosizer uses four timers for the TOF measurement. Only one clock is used in the APS to determine the TOF. This difference may be reflected in the noise level. The noise of both instruments arises when the PMT produces a signal that is not associated with a particle event, and this signal is detected as a particle passing through the sensing volume. The calculated particle size from a false signal depends on the true particle concentration, and the exact time sequence of this false signal. With a single clock system, the noises tend to produce more signals for small particles, whereas for the Aerosizer, the noise level appears to be uniform across the size range. Both instruments have an internal mechanism to reduce or correct for the background noise level. However, it is not completely removed and false signals affect the accuracy of the size distribution. Both the Aerosizer and the APS measure the size number distribution, but they also calculate the surface area and volume distributions, assuming that the particles are spherical. With noise corrections, false signals do not significantly affect the number distribution. However, when the same size distribution is transformed into a volume distribution, false signals in large particles are amplified. Therefore, the noise tends to skew the size distribution toward the large particles, especially in the Aerosizer.

The third feature of the Aerosizer that is different from the APS is the data presentation. Both instruments calculate the measured size distribution in terms of number, surface area, and volume distributions. The APS data are presented in the absolute units of particle number/cm^3, surface area/cm^3, and volume/cm^3, whereas the Aerosizer data are normalized with respect to the peak concentration. The Aerosizer distribution can be adjusted to give an estimated true concentration, but may be in error due to the way the background is subtracted from the TOF spectrum.

14.5 LIST OF SYMBOLS

C_c	Cunningham slip correction factor
d	droplet diameter
d_a	aerodynamic diameter
d_p	particle diameter
D_{API}	geometric diameter measured by the Aerosizer
D_g	true geometric diameter from microscopy
F_D	drag force
M	gas molecular weight
m_p	particle mass
ΔP	pressure drop across the nozzle; pressure drop
P	atmospheric pressure; ambient pressure
q	electrostatic charge
R	universal gas constant
S	transit time between laser beams; distance between the laser beams
Stk	Stokes number
T	absolute temperature; temperature in K
t	transit time [referred to as the time-of-flight (TOF)]
t_{min}	minimum transit time; minimum transit time for small particles at a fixed distance downstream of the nozzle
U	particle velocity relative to the air
U_g	gas velocity; gas velocity in the nozzle
V_g	air velocity at the nozzle exit

V_p	particle velocity
$V_{p(a)}$	particle velocity component due to the acoustic field
$V_{p(e)}$	particle velocity component due to the electric field
$V_{p(m)}$	particle velocity as measured
We	Weber number
Δ	mean free path of the gas molecules
γ	droplet surface tension; ratio of specific heat capacities (Eq. 14-38)
η	gas viscosity
η_a	sample aspiration; aspiration efficiency
η_d	detection efficiency
$\eta_{overall}$	overall counting efficiency; overall transmission efficiency
η_t	transmission efficiency
μ	gas dynamic viscosity
ω	frequency radians per second
ϕ	phase lag of the particle motion
τ_p	relaxation time
ρ_g	gas density
ρ_p	particle density

14.6 REFERENCES

Agarwal, A. R., and R. J. Ramiarz (1981). *Development of an Aerodynamic Particle Size Analyzer*. Cincinnati, OH, USDHEW-NIOSH.

Agranovski, V., and Z. D. Ristovski (2005). Real-time monitoring of viable bioaerosols: Capability of the UVAPS to predict the amount of individual microorganisms in aerosol particles. *J. Aerosol Sci.* 36(5–6): 665–676.

Ali, M., R. N. Reddy, and M. K. Mazumder (2008). Simultaneous characterization of aerodynamic size and electrostatic charge characterization of inhaled dry powder inhaler aerosol. *Curr. Resp. Med. Rev.* 4: 2–5.

Ananth, G., and J. C. Wilson (1988). Theoretical-analysis of the performance of the TSI aerodynamic particle sizer—The effect of density on response. *Aerosol Sci. Technol.* 9(3): 189–199.

Baron, P. A. (1986). Calibration and use of the aerodynamic particle sizer (APS 3300). *Aerosol Sci. Technol.* 5(1): 55–67.

Baron, P. A., and K. Willeke (1986). Respirable droplets from whirlpools—Measurements of size distribution and estimation of disease potential. *Environ. Res.* 39(1): 8–18.

Baron, P. A., J. M. Yacher, and W. A. Heitbrink (1996). Some observations on the response of the Aerosizer to droplets in the 4–18 μm range. Presented at the American Asssication for Aerosol Research Annual Conference, October, Orlando FL.

Baron, P., G. J. Deye, A. B. Martinez, E. N. Jones, and J. S. Bennett (2008). Size shifts in measurements of droplets with the aerodynamic particle sizer and the aerosizer. *Aerosol Sci. Technol.* 42(3): 201–209.

Bartley, D. L., P. A. Baron, A. B. Martinez, D. R. Secker, and E. Hirsch (2000). Droplet distortion in accelerating flow. *J. Aerosol Sci.* 31: 1447–1460.

Blackford, D., A. E. Hanson, D. Y. H. Pui, P. D. Kinney, and G. P. Ananth (1988). Details of recent work towards improving the performance of the TSI aerodynamic particle sizer. Second Annual Meeting of the Aerosol Society, Bournemouth, UK March 22-24.

Brosseau, L. M., D. Vesley, N. Rice, K. Goodell, M. Nellis, and P. Hairston (2000). Differences in detected fluorescence among several bacterial species measured with a direct-reading particle sizer and fluorescence detector. *Aerosol Sci. Technol.* 32(6): 545–558.

Caldow, R., F. R. Quant, R. L. Holm, and P. P. Hairston (1997). Design of a next-generation aerodynamic particle sizing time-of-flight spectrometer. Sixteenth Annual American Association for Aerosol Research Meeting, October, Denver, CO.

Chen, B. T., Y. S. Cheng, and H. C. Yeh (1985). Performance of a TSI aerodynamic particle sizer. *Aerosol Sci. Technol.* 4, 89–97.

Chen, B. T., Y. S. Cheng, and H. C. Yeh (1990). A study of density effect and droplet deformation in the TSI aerodynamic particle sizer. *Aerosol Sci. Technol.* 12: 278–285.

Chen, Y., E. M. Barber, and Y. Zhang (1998). Sampling efficiency of the TSI aerodynamic particle sizer. *Instrum. Sci. Technol.* 26(4): 363–373.

Chen, C. C., and S. H. Huang (1999). Shift of aerosol penetration in respirable cyclone samplers. *American Industrial Hygiene Association Journal* 60: 720–729.

Cheng, Y. S., and B. E. Dahneke (1979). Properties of continuum source particle beams. II. beams generated in capillary expansions. *J. Aerosol Sci.* 10: 363–368.

Cheng, Y. S., B. T. Chen, and H. C. Yeh (1990). Behaviour of isometric nonspherical aerosol particles in the aerodynamic particle sizer. *J. Aerosol Sci.* 21(5): 701–710.

Cheng, Y. S., E. B. Barr, I. A. Marshall, and J. P Mitchell (1993). Calibration and performance of an API Aerosizer. *J. Aerosol Sci.* 24: 501–514.

Clift, R., J. R. Grace, and M. E. Weber (1978). *Bubbles, Drops and Particles.* New York, Academic.

Dahneke, B. 1973. Aerosol beam spectrometry. *Nature Phys. Sci.* 244: 54–55.

Dahneke, B. E., and Y. S. Cheng (1979). Properties of continuum source particle beams I. calculation methods and results. *J. Aerosol Sci.* 10:257–274.

Dahneke, B., and D. Padliya (1977). Nozzle-inlet design for aerosol beam. *Instruments in Rarefied Gas Dynamics*, 51, Part II, pp. 1163–1172.

DeCarlo, P. F., J. G. Slowik, D. R. Worsnop, P. Davidovits, and J. L. Jimenez (2004). Particle morphology and density characterization by combined mobility and aerodynamic diameter measurements. Part 1: Theory. *Aerosol Sci. Technol.* 38(12): 1185–1205.

DiVito, W. J. (1998). Digital Acquisition and Demodulation of LDV Signal Bursts to Obtain Particle Size and Charge Data, PhD Dissertation, University of Arkansas at Little Rock, Little Rock, AR.

Drain, L. E. (1980). *The Laser Doppler Technique*. New York, John Wiley and Sons.

Durst, F., A. Melling, and J. H. Whitelaw (1981). *Principles and Practice of Laser-Doppler Anemometry*. New York, Academic.

Fuchs, N. A. (1964). *Mechanics of Aerosols*. New York, Pergamon.

Griffiths, W. D., P. J. Iles, and N. P. Vaughan (1986). The behavior of liquid droplet aerosols in an Aps-3300. *J. Aerosol Sci.* 17(6): 921–930.

Heitbrink, W. A., and P. A. Baron (1991). Coincidence in time-of-flight aerosol spectrometers: Phantom particle creation. *Aerosol Sci. Technol.* 53: 427–531.

Hinds, W. C. (1999). *Aerosol Technology: Properties, Behavior, and Measurement of Airborne Particles*, 2 ed. New York, Wiley-Interscience.

Jones, W., J. Jankovic, and P. A. Baron (1983). Design, Construction and Evaluation of a Multistage Cassette Impactor. *Am. Indust. Hyg. Assoc. J.* 44(6): 409–418.

Kanaani, H., M. Hargreaves, J. Smith, Z. Ristovski, V. Agranovski, and L. Morawska (2008). Performance of UVAPS with respect to detection of airborne fungi. *J. Aerosol Sci.* 39(2): 175–189.

Kenny, L. C., and R. A. Gussman (2000). A direct approach to the design of cyclones for aerosol-monitoring applications. *Journal of Aerosol Science* 31(12): 1407–1420.

Kenny, L. C., T. Merrifield, D. Mark, R. Gussman, and A. Thorpe (2004). The development and designation testing of a new USEPA-approved fine particle inlet: A study of the USEPA designation process. *Aerosol Science and Technology* 38: 15–22.

Kinney, P. D., and D. Y. H. Pui (1995). Inlet efficiency study for the TSI aerodynamic particle sizer. *Part. Part. Syst. Char.* 12: 188–193.

Kirsch, K. J., and Mazumder, M. K. (1975). Aerosol size spectrum analysis using relaxation time analyzer. *Appl. Phys. Lett.* 26(4): 193–195.

Lee, K. W., J. C. Kim, and D. S. Han (1990). Effects of gas-density and viscosity on response of aerodynamic particle sizer. *Aerosol Sci. Technol.* 13(2): 203–212.

Lee, S. J., P. Demokritou, and P. Koutrakis (2005). Performance evaluation of commonly used impaction substrates under various loading conditions. *Journal of Aerosol Science* 36(7): 881–895.

Lee, S. J., P. Demokritou, and P. Koutrakis (2006). Development and evaluation of personal respirable particulate sampler (PRPS). *Atmos. Environ.* 40(2): 212–224.

Lefebvre, A. H. (1989). *Atomization and Sprays*. Bristol, PA, Taylor and Francis.

Marshall, I. A., J. P. Mitchell, and W. D. Griffiths (1991). The behaviour of regular-shaped non-spherical particles in a TSI aerodynamic particle sizer. *J. Aerosol Sci.* 22(1): 73–89.

Maynard, A. D., L. C. Kenny, and P. E. J. Baldwin (1999). Development of a system to rapidly measure sampler penetration up to 20 μm aerodynamic diameter in calm air, using the aerodynamic particle sizer. *J. Aerosol Sci*. 30(9): 1215–1226.

Mazumder, M. K. (1970). Laser Doppler velocity measurement without directional ambiguity by using frequency shifted incident beams. *Appl. Phys. Lett.* 16(11): 462–464.

Mazumder, M. K., and K. J. Kirsch (1977). Single particle aerodynamic relaxation time analyzer. *Rev. Sci. Instrum.* 48(4): 622.

Mazumder, M. K., and Ware, R. E. (1987). Aerosol Particle Charge and Size Analyzer, US Patent 4633714.

Mazumder, M. K., R. E. Ware, J. D. Wilson, R. G. Renninger, F. C. Hiller, P. C. McLeod, R. W. Raible, and M. K. Testerman (1979). SPART analyzer: its application to aerodynamic size distribution measurements. *J. Aerosol Sci.* 10: 561–569.

Mazumder, M. K., R. E. Ware, and W. G. Hood (1983). Simultaneous measurements of aerodynamic diameter and electrostatic charge on single-particle basis. In *Measurements of Suspended Particles by Quasi-Elastic Light Scattering*, B. Dahneke (ed.). New York, John Wiley and Sons.

Mazumder, M. K., R. E. Ware, T. Yokoyama, B. J. Rubin, and D. Kamp (1991). Measurement of particle size and electrostatic charge distributions on toners using ESPART analyzer. *IEEE Trans. Ind. Appl.* 27(4): 611–619.

Mazumder, M. K., N. Grable, Y. Tang, S. O'Connor, and R. A. Sims (1999). Real-time particle size and electrostatic charge distribution analysis and its applications to electrostatic processes. *Inst. Phys. Conf. No. 163*. pp. 335–347.

Misra, C., M. Singh, S. Shen, C. Sioutas, and P. A. Hall (2002). Development and evaluation of a personal cascade impactor sampler (PCIS). *J. Aerosol Sci.* 33(7): 1027–1047.

Mu, Q. (1994). In-situ Measurements of Aerodynamic Size and Electrostatic Charge Distributions of Particles on a Powder Cloud by Image Analysis, PhD Dissertation, University of Arkansas at Little Rock, Little Rock, AR.

Oskouie, A. K., H.-C. Wang, R. Mavliev, and K. E. Noll (1998). Calculated calibration curves for particle size determination based on time-of-flight (TOF). *Aerosol Sci. Technol.* 29(5): 433–441.

Peters, T. M. (2006). Use of the Aerodynamic Particle Sizer to measure ambient PM10-2.5: the coarse fraction of PM10. *J. Air Waste Manag. Assoc.* 56: 411–416.

Peters, T. M., and D. Leith (2003). Concentration measurement and counting efficiency of the aerodynamic particle sizer 3321. *J. Aerosol Sci.* 34(5): 627–634.

Peters, T. M., H. M. Chein, D. A. Lundgren, and P. B. Keady (1993). Comparison and combination of aerosol size distributions measured with a low pressure impactor, differential mobility particle sizer, electrical aerosol analyzer, and aerodynamic particle sizer. *Aerosol Sci. Technol.* 19: 396–405.

Rader, D. J., J. E. Brockmann, D. L. Ceman, and D. A. Lucero (1990). A method to employ the aerodynamic particle sizer factory calibration under different operating-conditions. *Aerosol Sci. Technol.* 13(4): 514–521.

Reid, J. S., and T. M. Peters (2007). Update to "Reconciliation of coarse mode sea-salt aerosol particle size measurements and parameterizations at a subtropical ocean receptor site" regarding the use of aerodynamic particle sizers in marine environments. *J. Geophys. Res.-Atmos.* 112, D04202 http://www.agu.org/journals/jd/jd0704/2006JD007501/2006JD007501.pdf

Reid, J. S., H. H. Jonsson, H. B. Maring, A. Smirnov, D. L. Savoie, S. S. Cliff, E. A. Reid, J. M. Livingston, M. M. Meier, O. Dubovik, and S. C. Tsay (2003). Comparison of size and

morphological measurements of coarse mode dust particles from Africa. *J. Geophys. Res.-Atmos.* 108(D19): p–.

Sharma, R., D. W. Clark, P. K. Srirama, and M. K. Mazumder (2008). Contact charging of Martian dust simulant. *IEEE Trans. Indust. Applic.* 44(1): 32–39.

Sioutas, C., and E. Abt, J. M. Wolfson, and P. Koutrakis (1999). Evaluation of the measurement performance of the scanning mobility particle sizer and aerodynamic particle sizer. *Aerosol Sci. Technol.* 30: 84–92.

Slowik, J. G., K. Stainken, P. Davidovits, L. R. Williams, J. T. Jayne, C. E. Kolb, D. R. Worsnop, Y. Rudich, P. F. DeCarlo, and J. L. Jimenez (2004). Particle morphology and density characterization by combined mobility and aerodynamic diameter measurements. Part 2: Application to combustion-generated soot aerosols as a function of fuel equivalence ratio. *Aerosol Sci. Technol.* 38(12): 1206–1222.

Srirama, P. K., J. Zhang, J. D. Wilson, and M. K. Mazumder (2007). Mars dust: real time and in-situ measurements of size and charge distributions. Proceedings of the ESA Annual Meeting on Electrostatics, Purdue University, West Lafayette, IN, pp. 184–19.

Stanier, C. O., A. Y. Khlystov, S. N. Pandis, and N. Spyros (2004). Ambient aerosol size distributions and number concentrations measured during the Pittsburgh Air Quality Study (PAQS). *Atmos. Environ.* 38(20): 3275.

Stein, S., G. Gabrio, D. Oberreit, P. P. Hairston, P. B. Myrdal, and T. J. Beck (2002). An evaluation of mass-weighted size distribution measurements with the model 3320 aerodynamic particle sizer. *Aerosol Sci. Technol.* 36: 845–854.

Stein, S. W., P. B. Myrdal, B. J. Gabrio, D. Obereit, and T. J. Beck (2003). Evaluation of a new Aerodynamic Particle Sizer (R) spectrometer for size distribution measurements of solution metered dose inhalers. *Journal of Aerosol Medicine-Deposition Clearance and Effects in the Lung* 16(2): 107–119.

Thornburg, S., J. Cooper, and D. Leith (1999). Counting efficiency of the API Aerosizer. *J. Aerosol Sci.* 30: 479–488.

Tsai, C. J., H. M. Chein, S. T. Chang, and J. Y. Kuo (1998). Performance evaluation of an API Aerosizer. *J. Aerosol Sci.* 29: 839–853.

Tsai, C. J., S. C. Chen, C. H. Huang, and D. R. Chen (2004). A universal calibration curve for the TSI aerodynamic particle sizer. *Aerosol Sci. Technol.* 38(5): 467–474.

Volckens, J., and T. M. Peters (2005). Counting and particle transmission efficiency of the aerodynamic particle sizer. *J. Aerosol Sci.* 36: 1400–1408.

Wang, H.-C., and W. John (1987). Particle density correction for the aerodynamic particle sizer. *Aerosol Sci. Technol.* 6: 191–198.

Wang, H.-C., and W. John (1989). A simple iteration procedure to correct for the density effect in the aerodynamic particle sizer. *Aerosol Sci. Technol.* 10: 501–505.

Wilson, J. C., and B. Y. H. Liu (1980). Aerodynamic particle size measurement by laser-Doppler velocimetry. *J. Aerosol Sci.* 11: 139–150.